High probability neurotransmitter release sites represent an energy efficient design

Zhongmin, Lu; Chouhan, Amit K.; Rossano, Adam J; Brain, Keith; Zhou, You; Borycz, Jolanta A.; Lu, Zhiyaun; Meinertzhagen, Ian A.; Macleod, Gregory T.

DOI:
10.1016/j.cub.2016.07.032

Document Version
Peer reviewed version

Citation for published version (Harvard):
Zhongmin, L, Chouhan, AK, Rossano, AJ, Brain, KL, Zhou, Y, Borycz, JA, Lu, Z, Meinertzhagen, IA & Macleod, GT 2016, 'High probability neurotransmitter release sites represent an energy efficient design', Current Biology, vol. 26, no. 19, pp. 2562-2571. https://doi.org/10.1016/j.cub.2016.07.032

High probability neurotransmitter release sites represent an energy efficient design

Zhongmin Lu, Amit K. Chouhan, Jolanta A. Borycz, Zhiyuan Lu, Adam J. Rossano, Keith L. Brain, You Zhou, Ian A. Meinertzhagen, Gregory T. Macleod

PII: S0960-9822(16)30783-7
DOI: doi:10.1016/j.cub.2016.07.032
Reference: CURBIO 13036

Published in: *Current Biology*

Received date: 6 November 2015
Revised date: 6 June 2016
Accepted date: 12 July 2016

Cite this article as: Lu Z, Chouhan AK, Borycz JA, Lu Z, Rossano AJ, Brain KL, Zhou Y, Meinertzhagen IA, Macleod GT, High probability neurotransmitter release sites represent an energy efficient design, *Current Biology*, doi:10.1016/j.cub.2016.07.032

Highlights:

- We estimated the energy efficiency of individual motor nerve terminals *in situ*.
- Energy efficiency was calculated as glutamate release relative to ATP hydrolysis.
- Terminals with high probability neurotransmitter release sites are most efficient.
- Simulations indicate that most release sites operate well below optimal efficiency.

eTOC blurb:

High probability release sites are not uncommon, but what are their advantages? Lu et al. show that energy efficiency is one of their advantages. However, the probability value at any particular synapse might be seen as a trade-off between energy efficiency and other functional properties such as a capacity for sustained release.

Title: High probability neurotransmitter release sites represent an energy efficient design.

Authors / Affiliations: Zhongmin Lu[1], Amit K. Chouhan[2], Jolanta A. Borycz[3], Zhiyuan Lu[3], Adam J Rossano[4], Keith L. Brain[5], You Zhou[6], Ian A. Meinertzhagen[3], Gregory T. Macleod[7]

1 – Integrative Biology and Neuroscience Graduate Program, Department of Biological Sciences & Wilkes Honors College, Florida Atlantic University, Jupiter, Florida.

2 - School of Psychology and Neuroscience, University of St Andrews, St Andrews, Scotland, UK.

3 - Department of Psychology and Neuroscience, Dalhousie University, Halifax, Nova Scotia, Canada.

4 - Physiology & Biomedical Engineering, Mayo Clinic College of Medicine, Rochester, Minnesota.

5 - Institute of Clinical Sciences, College of Medical and Dental Sciences, University of Birmingham, Edgbaston, Birmingham, UK.

6 - Department of Cellular and Structural Biology, University of Texas Health Science Center at San Antonio, San Antonio, Texas.

7 - Department of Biological Sciences & Wilkes Honors College, Florida Atlantic University, Jupiter, Florida.

Contact: macleodg@fau.edu

Keywords: neurotransmitter release, active zones, probability, presynaptic, energy efficiency, evolutionary biology

Running Title: Energy efficiency of neurotransmitter release.

Summary

Nerve terminals contain multiple sites specialized for the release of neurotransmitters. Release usually occurs with low probability, a design thought to confer many advantages. High probability release sites are not uncommon but their advantages are not well understood. Here we test the hypothesis that high probability release sites represent an energy efficient design. We examined release site probabilities and energy efficiency at the terminals of two glutamatergic motor neurons synapsing on the same muscle fiber in *Drosophila* larvae. Through electrophysiological and ultrastructural measurements we calculated release site probabilities to differ considerably between terminals (0.33 vs. 0.11). We estimated the energy required to release and recycle glutamate from the same measurements. The energy required to remove calcium and sodium ions subsequent to nerve excitation was estimated through microfluorimetric and morphological measurements. We calculated energy efficiency as the number of glutamate molecules released per ATP molecule hydrolyzed, and high probability release site terminals were found to be more efficient (0.13 vs. 0.06). Our analytical model indicates that energy efficiency is optimal (~0.15) at high release site probabilities (~0.76). As limitations in energy supply constrain neural function, high probability release sites might ameliorate such constraints by demanding less energy. Energy efficiency can be viewed as one aspect of nerve terminal function, in balance with others, because high efficiency terminals depress significantly during episodic bursts of activity.

Introduction

The strength of a synaptic connection is a function of three parameters: the number (N) of release sites, or active zones (AZs), at which neurotransmitter is released; the average probability of release from each AZ (P_{AZ}); and the average amplitude of the postsynaptic response to each packet of neurotransmitter [1]. It is not known why AZs with either a low or high P_{AZ} exist at any particular terminal. A low P_{AZ} confers advantages such as a high capacity for information storage [2], resistance to depression [3, 4], and energy efficient information transfer at convergent synaptic inputs [5, 6]. Insofar as the advantages of a low P_{AZ} design confer organisms with selective fitness, selection pressures might promote a common low P_{AZ}. However, P_{AZ} varies greatly between presynaptic terminals [7-14]. While reasons for a non-zero P_{AZ} are readily evident, the occurrence of high P_{AZ} synapses causes us to question what advantages these might confer to offset those of low P_{AZ}.

We propose that presynaptic energy efficiency, defined as the number of glutamate molecules released for each ATP molecule hydrolyzed, is one of the advantages inherent in high P_{AZ} release sites. Multiple calcium ions (Ca^{2+}) are required to trigger the release of neurotransmitters and this generates a steep dependency of P_{AZ} on Ca^{2+} entry, described as a sigmoid function [15]. As the cost of Ca^{2+} removal is one of the primary costs of the presynaptic terminal [16, 17] we might expect that energy efficiency will be optimized when neurotransmitter release is maximized relative to Ca^{2+} entry. This point does not occur until gains in neurotransmitter release become marginal relative to Ca^{2+} entry, i.e. high on the sigmoid curve, synonymous with high P_{AZ}.

Here we used direct measurements to make the first bottom-up estimates of presynaptic energy efficiency at individually identified neurons. We took advantage of two motor neurons that stereotypically innervate a single muscle fiber in *Drosophila* larvae. One neuron forms a small terminal with few AZs while the other forms a larger terminal with more AZs. We established that P_{AZ} differs considerably between the two terminal types. We then proceeded to test the hypothesis that high P_{AZ} confers high energy efficiency, estimating energy consumption through direct measurements of neurotransmitter release and Ca^{2+} entry, and by estimating sodium ion (Na^{+}) entry theoretically. We found that in response to an isolated AP the small terminal with high P_{AZ} was significantly more efficient, consistent with our hypothesis. Data collected during AP bursts supported the same hypothesis, but revealed that a high efficiency design based on high P_{AZ} will not sustain high output.

Results

QUANTIFICATION OF RELEASE SITE PROBABILITY (P_{AZ})

We set out to measure the average probability of release from AZs (P_{AZ}) at each of two glutamatergic motor neuron (MN) terminals that synapse on muscle fiber #6 (**Figure 1A**). Average P_{AZ} can be determined using **Equation 1**:

$$P_{AZ} = QC / N_{AZ} \quad (1)$$

where the number of packages of glutamate released [quantal content (QC)] by each terminal is determined electrophysiologically, and the number of AZs (N_{AZ}) determined by microscopy.

Type-Is terminals have fewer active zones than type-Ib

Muscle fiber #6 in *Drosophila* larvae is innervated by type-Is "small" bouton terminals of MNSNb/d-Is [18], and type-Ib "big" bouton terminals of MN6/7-Ib [19, 20]. The distinct identities of the live MN terminals are illustrated by differentially filling them with two fluorophores (**Figure 1A**). In fixed tissue, anti-horseradish peroxidase (HRP; [21]) was used to define neuronal membrane, anti-Bruchpilot (Brp; nc82; [22]) to identify AZs, and anti-Discs Large (DLG; [23]) to label the sub-synaptic reticulum (SSR) in the muscle and facilitate discrimination between boutons of different terminal types (**Figure 1B** and **Figures S1A** and **S1B**). Type-Is terminals on muscle 6 have a smaller surface area (Is: 234±110; Ib: 568±70 μm^2; N=6 pairs, SD, P<0.001; **Figure 1C; Table S1**) and volume (Is: 90±49; Ib: 310±49 μm^3; N=6 pairs, SD, P<0.001; **Figure 1D; Table S1**) than type-Ib terminals.

The number of AZs per unit volume was determined by counting AZ profiles in a series of transmission electron micrographs of 100 nm sections (**Figure 1E** and **1F**). The entire extent of each terminal was too large to reconstruct and we relied instead on synaptic vesicle (SV) sizes rather than morphologies to identify terminals because SV diameters differ between terminal types [24] (**Figure S1C**). Counts of AZ profiles per unit volume revealed a similar AZ density in the two terminal types (**Figure 1F; Table S1**). We estimated N_{AZ} for each of 6 terminals examined by light microscopy, multiplying its volume by the average number of AZs per unit volume. Average N_{AZ} was lower for type-Is terminals (Is: 223±66; Ib: 747±114 AZs; SEM; **Figure 1G; Table S1**).

Type-Is terminals release more neurotransmitter than type-Ib terminals

Quantal content (QC) can be determined for all AZs of each terminal type using an electrophysiological recording protocol that takes advantage of our knowledge of the stereotypical innervation of the body wall muscle fibers (see **Experimental Procedures** and **Figure 2A**). The

dependence of SV release on extracellular Ca^{2+} concentration ($[Ca^{2+}]_o$) was initially quantified in a low range of $[Ca^{2+}]_o$ (0.3-0.5 mM) in Hemolymph-Like solution #6 (HL6) [25] and type-Is terminals were found to have a much larger QC, i.e. they release more SVs across this range of $[Ca^{2+}]_o$ (**Figure S2A-S2D**). However, to quantify SV release under physiological conditions, $[Ca^{2+}]_o$ was raised to 2 mM $[Ca^{2+}]_o$ and synaptic events recorded under two-electrode voltage clamp (**Figure 2B**). Type-Is Excitatory Junction Currents (EJCs) were significantly larger than type-Ib EJCs (Is: 80.8±4.0, N=17; Ib: 59.9±3.1 nA; N=15, SEM, P<0.001; **Figure 2C**), but QC estimates were similar (QC: Is: 72.9±4.8; Ib: 80.6±4.5; SEM, P=0.25; **Figure 2D; Table S1**) after adjustments were made for the larger miniature EJPs (mEJCs) that originate from type-Is terminals (~50% larger, see **Experimental Procedures**). QC determined in another commonly used saline [Hemolymph-Like solution #3 (HL3)] [26] using physiological $[Ca^{2+}]_o$ gave similar results (**Figure S2E**). The capacity of each terminal to release glutamate beyond amounts recorded at physiological $[Ca^{2+}]_o$ was demonstrated by decreasing $[Mg^{2+}]_o$ in HL6 from 15mM to 10mM; EJC amplitude increased by 15.3% at both terminals (Is: 93.2±6.01; Ib: 69.8±4.18 nA; N=7, SEM, P<0.01).

Type-Is terminals have a higher P_{AZ} than type-Ib

P_{AZ} was estimated for each terminal using **equation 1** and the estimates of QC made in 2 mM $[Ca^{2+}]_o$ HL6. P_{AZ} was 3-fold higher for type-Is terminals than for type-Ib terminals (Is: P_{AZ} = QC / N_{AZ} = 72.9/223 = 0.33±0.10; Ib: P_{AZ} = 80.6/747 = 0.11±0.02; SEM) (**Figure 2E; Table S1**). The assumption that all AZs identified from EM are functional, is favored over the alternative that only AZs with T-bars (**Figure S1D**) are functional, because the latter assumption generates P_{AZ} estimates > 1 in type-Is terminals (Is: P_{AZ} = 72.9/59 = 1.24; Ib: P_{AZ} = 80.6/421 = 0.19).

QUANTIFICATION OF PRESYNAPTIC ENERGY EFFICIENCY

Our conception of energy efficiency is based on Maxwell's definition [27], based on output relative to input (see **Experimental Procedures)**. To test our hypothesis that high P_{AZ} terminals are more energy efficient we must estimate the number of glutamate molecules released from each terminal relative to the amount of energy required to release and recycle the glutamate and to remove Ca^{2+} and Na^+. The QC estimates above contribute to an estimation of both the number of glutamate molecules released and the number of ATP molecules needed to recycle the glutamate and SVs. Next, microfluorimetric measurements in conjunction with our morphological data were used to quantify Ca^{2+} number, and a theoretical approach based on those data used to quantify Na^+ number. These estimates for Ca^{2+} number and Na^+ number were then used to estimate the numbers of ATP molecules required to power Ca^{2+} and Na^+ removal.

Glutamate Handling

Type-Is terminals release the most glutamate during an AP

The number of glutamate molecules released in response to a single AP (Glu) can be determined using **equation 2**:

$$Glu = QC \times \varepsilon \quad (2)$$

where QC is the number of SVs released, determined above (**Figure 2D**), and ε is the number of glutamate molecules in a SV. Values for ε were estimated for SVs in each terminal type by combining a nominal value of ε generated in a biophysical study at the *Drosophila* larval NMJ [28] and scaling factors derived from amplitude differences in uni-quantal events produced by each terminal (ε; Is: 9600; Ib: 6400 molecules). Using **Equation 2**, we calculated that type-Is terminals release more glutamate per AP [Is: (7.00±0.46) x 10^5; Ib: (5.16±0.29) x 10^5 glutamate molecules; SEM] (**Table S1**).

The number of ATP molecules required to recycle and refill SVs with glutamate after an AP (E_{Glu}) can be determined using **equation 3**:

$$E_{Glu.} = QC \times 410.5 + Glu \times 2.67 \quad (3)$$

where the estimated cost of exocytosis and endocytosis of a single SV of measured diameter is 410.5 ATP molecules [29], and it costs 2.67 ATP molecules to load a glutamate molecule into a SV. The value of 410.5 has been adopted for SVs of both terminals. For a single AP, type-Is terminals spend more ATP recycling and refilling SVs with glutamate [Is: (1.90±0.12) x 10^6; Ib: (1.41±0.08) x 10^6 ATP molecules; SEM] (**Table S1**).

Calcium Handling

The number of calcium ions (Ca^{2+}_{total}) that enter each terminal during an AP can be determined using **equation 4:**

$$Ca^{2+}_{total} = \Delta[Ca^{2+}]_{total} \times vol \times A_N \quad (4)$$

where $\Delta[Ca^{2+}]_{total}$ is the change in total Ca^{2+} concentration (free+bound) (moles / L), vol is the volume of the terminal (L) which has been determined (**Figure 1D**), and A_N is Avogadro's constant, but

$\Delta[Ca^{2+}]_{total}$ must be calculated using **equation 5** [(equation 4) of [30]]:

$$\Delta[Ca^{2+}]_{total} = \Delta[Ca^{2+}]_{AP} \times (1 + K_S + K'_B) \quad (5)$$

where $\Delta[Ca^{2+}]_{AP}$ is the change in cytosolic free Ca^{2+} concentration ($[Ca^{2+}]_i$) in response to a single AP, K_S is the endogenous Ca^{2+} binding ratio, and K'_B the incremental Ca^{2+} binding ratio for the exogenous Ca^{2+} buffer, Oregon-Green BAPTA-1 (OGB-1).

Type-Is terminals display the largest transients in cytosolic free Ca^{2+} concentration

We determined changes in $[Ca^{2+}]_i$ by forward-filling terminals with a mixture of a Ca^{2+} sensitive fluorescent dye and a Ca^{2+}-insensitive fluorescent dye, in a constant ratio (~15:1; OGB-1 dextran : AF647 dextran) (**Figure 3**). A single AP evoked a greater increase in OGB-1 fluorescence, and thus $[Ca^{2+}]_i$, in type-Is terminals than type-Ib (Is: 412.3±59.9; Ib, 292.1±34.2 nM; N=12 pairs, SEM, $P<0.05$; **Figure 3B** and **3C**). See **Experimental Procedures** for calibration of the ratio against $[Ca^{2+}]_i$. The time course of decay (τ) of $[Ca^{2+}]_i$ was similar between terminal types (Is: 75.9±4.7; Ib: 75.3±6.5 ms; SEM; **Figure S3A** and **S3B**), and the time integral of the $[Ca^{2+}]_i$ transient ($\Delta[Ca^{2+}]_{AP} \cdot \tau$), was greater in type-Is terminals (Is: 28.9±3.2; Ib: 20.2±1.7 nM·s; SEM, $P<0.05$; **Figure S3C**). The endogenous Ca^{2+} binding ratio (K_S) was calculated as described in the **Experimental Procedures** (K_S: Is: 82, Ib: 49; **Figure S3D** and **S3F**). Using equation 5 we calculated the change in total $[Ca^{2+}]_i$ ($\Delta[Ca^{2+}]_{total}$) to be significantly greater in type-Is terminals (Is: 40.1±5.5; Ib: 20.6±2.2 μM; SEM, $P<0.05$; **Figure 3D**).

Type-Is terminals admit the least Ca^{2+}

The number of calcium ions that enter the entire terminal during an AP (Ca^{2+} total) was calculated using equation 4. This analysis revealed that total Ca^{2+} entry is least for type-Is terminals [Is: (2.18±0.57) x 10^6; Ib: (3.86±0.49) x 10^6 ions; SEM; **Figure 3E**] consistent with their 3.5 fold smaller volume, despite a 2-fold greater $\Delta[Ca^{2+}]_{total}$. Significantly, Ca^{2+} entry per-unit-volume was much higher in type-Is terminals (Is: 2.42 x 10^4; Ib: 1.24 x 10^4 ions / μm^3; SEM), consistent with their larger $[Ca^{2+}]_i$ transients (**Figure 3B** and **3C**), despite their higher estimated K_S. We also estimated Ca^{2+} entry per AZ, as this is most likely to vary in proportion with microdomain Ca^{2+} concentration which is most relevant to the Ca^{2+} sensor at the AZ. Ca^{2+} entry per AZ is greater for type Is terminals [Is: (9.77±3.87) x 10^3; Ib: (5.17±1.02) x 10^3 ions; SEM; **Table S1**] and this provides a simple explanation for the higher P_{AZ} of type-Is terminals.

The number of ATP molecules required to extrude the Ca^{2+} that enters during an AP ($E_{Ca^{2+}}$) can be calculated using **equation 6**:

$$E_{Ca^{2+}} = Ca^{2+}_{total} \times 1 \text{ ATP} / 1 Ca^{2+} \quad (6)$$

where 1 ATP molecule is required to extrude 1 calcium ion regardless of its route of exit [29]. Type-Is terminals were found to spend far less ATP on Ca^{2+} extrusion per AP [Is: (2.18±0.57) x 10^6; Ib: (3.86±0.49) x 10^6 molecules; SEM] (**Figure 4A** and **4B; Table S1**).

Sodium Handling

Type-Is terminals require the least Na^+ current to depolarize

An indirect estimate of the minimum Na^+ entering the presynaptic terminal during an AP can be calculated using **equation 7**:

$$q = V \times C \quad (7)$$

where a charge (q; Coulombs) is needed to change the voltage (V; volts) across the capacitance (C; uF) of presynaptic membrane by the amplitude of the AP [29, 31, 32]. The AP amplitude was taken as a nominal 100 mV, specific membrane capacitance as 1 μF/cm^2, and the area was estimated from confocal microscopic examination (Is: 234±110; Ib: 568±70 μm^2; SD; **Figure 1C**). The resulting estimate of Na^+ charge entry (Na^+_{total}) had to be multiplied by an "overlap factor" representing the degree to which K^+ entry works against Na^+ entry during the rising phase of the AP [29, 31-33]. Patch recordings have not been made from *Drosophila* glutamatergic MN terminals, but an estimate of 3.05 comes from Kenyon cell axons of the honeybee, *Apis mellifera* [34]. The resulting estimates of Na^+ entry showed that considerably more Na^+ was expected to enter the larger type-Ib terminals [Is: (0.45±0.09) x 10^7; Ib: (1.08±0.06) x 10^7 Na^+ ions; SEM; **Table S1**].

The number of ATP molecules required to extrude Na^+ (E_{Na^+}) can be calculated using **equation 8**:

$$E_{Na^+} = Na^+_{total} / 3 \text{ ATP} \quad (8)$$

where 1 ATP molecule can extrude 3 sodium ions [29]. Type-Is terminals were found to spend far less ATP on Na^+ extrusion per AP [Is: (1.48±0.28) x 10^6; Ib: (3.60±0.18) x 10^6 ATP molecules; SEM; **Figure 4A** and **4B; Table S1**].

Type-Is terminals, with the highest P_{AZ}, release neurotransmitter with the highest efficiency

The total number of ATP molecules (E_{total}) required to release and recycle glutamate and to remove Ca^{2+} and Na^{+} after a single AP can be calculated using **equation 9**:

$$E_{total} = E_{Glu} + E_{Ca^{2+}} + E_{Na^{+}} \quad (9)$$

where E_{Glu}, E_{Ca2+} and E_{Na+} were determined above. Although type-Is terminals release more glutamate per AP [Glu: Is: (7.00±0.46) x 10^5; Ib: (5.16±0.29) x 10^5 glutamate molecules; SEM] (**Figure 4A** and **4B; Table S1**), they expend less ATP in doing so [E_{total}: Is: (5.56±0.65) x 10^6; Ib: (8.88±0.52) x 10^6 ATP molecules; SEM] (**Figure 4A** and **4B; Table S1**), primarily because they need to spend less ATP extruding Ca^{2+} and Na^{+}. Energy efficiency (E.E.) can be calculated using **equation 10**:

$$E.E. = Glu / E_{total} \quad (10)$$

where, Glu and E_{total} have already been determined. Expressed in terms of the number of glutamate molecules released for each ATP molecule hydrolyzed, type-Is terminals are twice as efficient as type-Ib (Is: 0.126±0.017; Ib: 0.058±0.005; SEM; **Figure 4C; Table S1)**. The hydrolysis of ATP to ADP under conditions that might be found within the cells of an invertebrate yields ~56.1 kJoules / mol [35] and so the efficiency values above might be re-expressed in terms of Joules consumed per glutamate molecule released (Is: 0.74 x 10^{-18}; Ib: 1.61 x 10^{-18}) or mole of glutamate released (Is: 4.45 x 10^5; Ib: 9.67 x 10^5).

A test of the "relative" energy efficiency of nerve terminals, one which does not rely on the accuracy of estimates for the amount of ATP, but rather on parameters measured directly in this study, is the number of SVs released relative to the amount of Ca^{2+} pumped [Is: (3.35±0.90) x 10^{-5}; Ib: (2.09±0.29) x 10^{-5}; SEM; **Table S1**], or the number of glutamate molecules released per number of Ca^{2+} ions that enter (Is: 0.321±0.087; Ib: 0.134±0.018; SEM; **Table S1**). In both cases, far less Ca^{2+} is required for type-Is terminals, reaffirming our conclusion that type-Is terminals with a high P_{AZ} embody a more energy efficient design for releasing glutamate.

SIMULATION OF PRESYNAPTIC ENERGY EFFICIENCY

Although our data support the hypothesis that high P_{AZ} confers greater energy efficiency, it relies on measurements from the terminals of just two MNs and is therefore not a powerful test. To further

explore the influences on presynaptic energy efficiency we built an analytical model based on the data collected from the two MN terminals (**Appendix I**). This model allowed us to examine the influence of systematically altering various aspects of presynaptic morphology, physiology and biochemistry on presynaptic energy efficiency during a single AP.

P_{AZ} itself can be expressed as a function of 3 parameters (**Appendix I**): Ca^{2+} entry per AZ; Ca^{2+} sensitivity of the trigger for exocytosis (S); and cooperativity between Ca^{2+} binding sites on the trigger (n_H; [15, 36]). Simulation of changes in the magnitude of each parameter, while holding the other parameters constant, demonstrates that P_{AZ} is highly responsive to changes in Ca^{2+} entry per AZ and even more responsive to n_H (**Figure 5A**). Simulating the influence of S, n_H, N_{AZ}, Ca^{2+} entry per AZ and SV size on glutamate release we see that Ca^{2+} entry per AZ and n_H are again highly influential (S, n_H & Ca^{2+}/AZ: **Figure 5B**; N_{AZ}, SV size: **Figure S4A**). Total Ca^{2+} influx was sensitive to changes in Ca^{2+} entry per AZ and N_{AZ} but not n_H, S or SV size (**Figure S4B**). Total Na^+ entry was sensitive to a different set of parameters, such as surface area and a number of parameters for which no direct data are available for *Drosophila* terminals; AP overlap factor, unit capacitance and AP voltage change (**Figure S4C**).

We simulated the influence of each parameter on energy efficiency in **Figure 5C** and **S4D**. Glutamate release was unconstrained (as in **Figure 5B**) and each parameter systematically changed relative to measured values. Terminal size influences efficiency not through volume, but rather, through surface area, because it influences capacitance and the amount of Na^+ current required for depolarization. An increase in N_{AZ} leads to a greater increase in efficiency only because more glutamate will be released while Na^+ entry remains fixed (as terminal surface area is fixed). Also in **Figure 5C**, we see that parameters of n_H and Ca^{2+} entry per AZ, as well as S, are again highly influential.

It is unclear how variable the parameters underlying P_{AZ} may be in the program of any MN, but certainly *Drosophila* MN terminals have the capacity to change Ca^{2+} entry within minutes in response to an unconditioned AP [37]. Simulation of the effect of increasing Ca^{2+} entry per AZ to increase P_{AZ} shows that both terminals can improve their efficiency in the short term by as much as 25% for type-Is terminals and 150% for type-Ib (**Figure 5D**). The corresponding P_{AZ} for energy efficiency maximization is high in both terminals (Is: 0.76; Ib: 0.73). Energy efficiency will be maximized immediately before the point at which the incremental cost of releasing one more glutamate molecule exceeds the average cost of glutamate already released, a point high on the sigmoid curve that represents the dependence of glutamate release on Ca^{2+} entry per AZ (**Figure 5D**, **inset**, **arrowheads**).

QUANTIFICATION OF PRESYNAPTIC ENERGY EFFICIENCY DURING MOTOR PATTERNS

While a single MN AP is sufficient to elicit twitch in the muscle fiber, MNs cause muscle contractions relevant to locomotion through bursts of APs called motor patterns [38]. Nerve terminals containing high P_{AZ} release sites commonly show a depressing release profile during trains of APs, while those with low P_{AZ} release sites show a facilitating profile [3]. It seems possible then that if the high P_{AZ} terminals depress sufficiently then differences in efficiency between terminals may disappear. Energy efficiency during bursts of activity ($E.E._{.bursts}$) can be calculated using **equation 11**:

$$E.E._{.bursts} = Glu_{bursts} / E_{total\text{-}bursts} \quad (11)$$

where, Glu_{bursts} is quantified as Glu for an AP in the middle of a 2 s train of stimuli delivered at the endogenous firing rate (EFR), and $E_{total\text{-}bursts}$ is the total number of ATP molecules required to "support" neurotransmitter release and recycling, and Ca^{2+} and Na^{+} regulation.

High-efficiency type-Is terminals fire at the lowest rate

To determine the endogenous firing rate (EFR) of each MN during motor patterns we recorded synaptic activity from adjacent muscle fibers (**Figure 6A**) while the central pattern generator (CPG) drove activity (**Figure 6B**), an experimental condition referred to as fictive locomotion. Using a previously described method [39] we were able to determine the EFR for each of the two MNs (see also **Figures S5A** and **S5B**). The EFR was significantly lower for MNSNb/d-Is than for MN6/7-Ib (Is: 7.8±0.7Hz; Ib: 20.7±0.8Hz; SEM, $P<0.001$; 2mM $[Ca^{2+}]_o$) (**Figure S5C**).

High-efficiency terminals show the greatest frequency depression

When firing was driven at 10Hz (**Figure 6C-6D**), close to the MNSNb/d-Is EFR of 7.8Hz, type-Is terminals show greater frequency depression of EJCs than type-Ib (Is: 37.9±1.5% mid-train, N=27; Ib: 8.0±2.2% mid-train, N=8; SEM, $P<0.001$; **Figure S5E**). When driven at 22Hz, close to the MN6/7-Ib EFR of 20.7Hz, frequency depression was not significantly greater in type-Ib terminals (**Figure 6D** and **Figures S5D** and **S5E**; 10.5±6.0% mid-train; N=6, SEM), demonstrating their robust capacity to sustain neurotransmitter release. After one second of activity (mid-train) at their respective EFRs, EJC amplitudes were similar between terminal types (Is: 48.5±10.8, N=20; Ib, 47.4±6.0 nA, N=6; SD; **Figures 6D** and **S5F**), yielding the following QC estimates (Is: 42.3±9.4; Ib, 62.1±7.9; SD, $P<0.05$), after adjusting for differences in mEJC amplitudes. Similar amounts of glutamate were released by the two terminals during a mid-train AP (Glu_{bursts}) (**Figure 6E**; **Table S2**) but type-Ib released much more glutamate per unit time (s) [calculated as the product of Glu_{bursts} and the EFR (**Figure 6F**; **Table**

S2)]. The ATP required to support presynaptic activity ($E_{total\text{-}bursts}$) per unit time ($E_{total\text{-}bursts}$ / s) may be represented as the sum of $E_{Glu\text{-}bursts}$ / s, $E_{Ca2+\text{-}bursts}$ / s and $E_{Na+\text{-}bursts}$ / s, as shown in **Figure 6G**.

High efficiency terminals show the greatest deterioration in efficiency during bursts

With estimates of Glu_{bursts} and $E_{total\text{-}bursts}$, **equation 11** was used to calculate energy efficiency during bursts ($E.E._{.bursts}$). Efficiency diminished, from single AP levels of 0.126±0.017 and 0.058±0.005 for terminal types-Is and -Ib respectively, to 0.085±0.020 and 0.046±0.009, respectively. The most significant decrease occurred in type-Is terminals (Is: 32.5% decline; Ib: 20.7% decline), resulting from their greater frequency depression. Unlike glutamate release from one AP to the next, we have assumed that there is no change in Ca^{2+} or Na^{+} entry from one AP to the next. Despite greater frequency depression in type-Is terminals, the difference in efficiency between terminals does not readily diminish during bursts of activity.

High-efficiency terminals fire only for short durations during fictive locomotion

To estimate each terminal's neurotransmitter output rate in a freely moving larva, MN duty cycle estimates are required. Peristaltic body wall contractions occur at a frequency of ~1 Hz in freely moving larvae [40], but the duty cycle of MN6/7-Ib and MNSNb/d-Is during locomotion is not known. Electrophysiological recordings during fictive locomotion reveal that MN6/7-Ib is active 5/6 of the contraction cycle [40], but no estimates are available for MNSNb/d-Is. To estimate the relative duty cycle of the terminals we adopted an optical approach monitoring changes in cytosolic GCaMP5 florescence as a proxy for electrical activity (**Figure 7A** and **7B**). Muscle contractions were blocked by adding 7mM glutamate to the saline [41]. Type-Ib terminals were active for a greater proportion of the time than type-Is terminals (Is: 0.074±0.024; Ib: 0.289±0.098; N=6, SD, P<0.001; **Figure 7B**).

High efficiency terminals likely have a low output in freely moving larvae

Glutamate release per unit time (Glu / $s_{loco.}$) and total ATP consumption per unit time (E_{total} / $s_{loco.}$) can be estimated in freely moving larvae using **Equations 12** and **13**:

$$Glu / s_{loco.} = Glu_{bursts} \times EFR \times D.C. \quad (12)$$

$$E_{total} / s_{loco.} = E_{total\text{-}bursts} \times EFR \times D.C. \quad (13)$$

where D.C. represents Duty Cycle (Is: 5/6 s x 0.074/0.289 = 0.213 s; Ib: 5/6 x 1 = 0.833 s, **Table S2**). Type-Ib terminals release over 10 fold more neurotransmitter per unit time (Glu / $s_{loco.}$; Is: (6.8±1.1) x

10^5; Ib: (68.5±10.4) x 10^5 glutamate molecules / s; SEM; **Figure 7C**) but require almost 18 fold more ATP to do so (E_{total} / $s_{loco.}$; Is: (7.9±1.3) x 10^6; Ib: (147.4±16.1) x 10^6 ATP/s; SEM; **Figure 7D**). This difference during endogenous activity is stark and to be able to sustain release at such high levels type-Ib terminals appear to pay a premium in having a low efficiency (**Figures 6G** and **7E**).

Given the large difference in the rate of output for each terminal, the question arises as to the ATP demand per unit volume to sustain these relative rates. Despite being much larger, ATP is required at a rate 5 times faster per unit volume in type-Ib terminals [Is: (8.8±2.4) x 10^4; Ib: (47.5±6.1) x 10^4 ATP molecules/μm^3/s; SEM]. The implication is that terminal volume is itself not rate limiting for neurotransmitter release from type-Is terminals.

In this study we only quantified the output of each MN on a single muscle fiber, but MN6/7-Ib innervates another muscle fiber and MNSNb/d-Is innervates seven other muscle fibers [18]. As neurotransmitter output on the other fibers is similar (data not shown), and terminals from the same axon all fire with the same frequency and duty cycle, we can estimate the summed glutamate for each MN. The glutamate output from all eight MNSNb/d-Is terminals is still less than the output from the two MN6/7-Ib terminals (60% less; **Figure 7C** arrows), and total ATP consumption would be considerably less (**Figure 7D** arrows).

Discussion

We report the relationship between P_{AZ} and energy efficiency in terminals of two glutamatergic MNs innervating the same target muscle fiber. P_{AZ} was three times higher in one of the terminals and this terminal was also twice as efficient, indicating that a high probability release site is more energy efficient. Given that the brain's energy demands are high [29], selection away from low P_{AZ} synapses because of their low efficiency might be expected to favor the adoption of a uniform high P_{AZ} design. However, we found that P_{AZ} values *in situ* fell short of the high P_{AZ} values predicted for optimal energy efficiency. Terminals with the lowest P_{AZ} and lowest energy efficiency depressed the least at endogenous release rates and performed most of the work during fictive locomotion. Our interpretation of these data is that selection away from energy inefficiency has favored high P_{AZ} but that increased P_{AZ} is held in check by selection away from an inability to sustain release.

Energy efficiency optimization as a selective pressure for high P_{AZ}

Selection away from energy inefficiency is thought to have influenced the size and other properties of synapses [42, 43], and in turn limited neural computational power [5, 44]. Here we suggest that selection away from energy inefficiency has selected for high P_{AZ} synapses, and we have demonstrated a positive correlation between P_{AZ} and energy efficiency under physiological conditions. High P_{AZ} can result from high Ca^{2+} entry/AZ, sensitivity (S) or cooperativity (n_H) of release [15, 36]. At first glance, these parameters seem to have qualitatively different influences on energy efficiency. High S or n_H lead to higher P_{AZ}, and, in turn, higher P_{AZ} leads to higher energy efficiency. More Ca^{2+} entry/AZ also results in higher P_{AZ}, but simulation of how changes in Ca^{2+} entry/AZ affect energy efficiency produced a curve with a distinct optimum. Further analysis revealed that energy efficiency would be optimized if P_{AZ} were elevated to 0.76 by an increase in Ca^{2+} entry/AZ. Taken together these simulation results show that a nerve terminal needs a relatively high P_{AZ} for optimal energy efficiency, but that efficiency diminishes at the highest P_{AZ} values because the purchase of more Ca^{2+} yields no more neurotransmitter release in return.

Trade-offs between presynaptic energy efficiency and function determine P_{AZ}

Trade-offs between energy efficiency and function have been observed previously [42, 45-47]. For relay synapses such as the NMJ, the trade-off appears to be between presynaptic energy efficiency and the capacity to sustain neurotransmitter release. Some mammalian central synapses show a capacity for sustained release and are exclusively low P_{AZ} synapses [48-51]. Here, we find that low P_{AZ} terminals depressed less than high P_{AZ} terminals, consistent with previous studies showing that low P_{AZ} synapses are likely to facilitate, whereas high P_{AZ} synapses are likely to depress [3]. Type-Ib

terminals with an endogenous firing rate of about 20 Hz offset the risk of depletion with a low P_{AZ}, but this measure is attended by low efficiency. The selection potential for low P_{AZ} becomes apparent when, in combination with large N_{AZ}, it confers a capacity to sustain high levels of release, which may translate to sustaining organismal locomotion without fatigue.

Presynaptic energy consumption in the context of postsynaptic energy consumption

While there is a clear rationale for selection against presynaptic design unable to sustain release at a NMJ, the rationale for selection against presynaptic energy inefficiency at a NMJ assumes that the presynaptic terminal consumes (or once consumed) a non-negligible proportion of the NMJ energy budget. Postsynaptic energy consumption can be estimated from EJC measurements that allow calculation of the amount of charge crossing the postsynaptic plasmamembrane in response to neurotransmitter released during a single presynaptic AP and the amount of ATP then needed to remove those ions (see **Supplemental Information**). Several assumptions that are difficult to defend have to be made to assess postsynaptic energy consumption (Is: 8.16×10^8, and, Ib: 5.18×10^8 ATP molecules). Yet, even if correct only in order of magnitude, we would conclude that the presynaptic terminal consumes ~1% of the NMJ energy budget. This proportion contrasts starkly with estimates at mammalian central synapses, at which presynaptic energy demands are ~30% of the total synaptic signaling cost [16, 17]. If presynaptic terminals only consume 1% of the NMJ energy budget we suggest that the ability to locomote without fatigue ultimately conferred a greater selection advantage than the energy saved by an efficient terminal, and that as a result low P_{AZ} release sites persisted at the expense of high P_{AZ} sites.

Figure Legends

Figure 1. Small motor neuron terminals (type-Is) have fewer active zones than large terminals (type-Ib). A, A confocal micrograph of fluorescence from terminals of two different motor neurons (MNSNb/d-Is and MN6/7-Ib) innervating muscle fibers #6 and #7. Both MNs express GFP, but the terminal of MNSNb/d-Is is filled with a greater concentration of AF647-dextran (magenta). **B-D**, Total terminal surface area and volume quantified on fiber #6 quantified from confocal microscopy. **B**, Fixed preparations immunolabelled to reveal the neuronal plasmamembrane [PM, (Horseradish Peroxidase, HRP)], the postsynaptic sub-synaptic reticulum [SSR, (Discs Large, DLG)] and active zones [AZs, (Bruchpilot, nc82)]. A series of images collected while advancing through the entire depth of the terminals, then collapsed into a maximal intensity z-projection stack viewed as an inverted grayscale. **C** and **D**, Plots of the total terminal surface area and volume for 6 different pairs of terminals. Averages shown as open circles (*, $P<0.001$, paired Student's t-test). SD shown in C and D. **E**, Transmission electron micrograph of a 100nm thick section through a type-Ib bouton on fiber #6 collected at 11,500X. AZs are evident with (arrow) and without (arrowhead) accompanying T-bars. **F**, The number of AZs per unit volume was plotted for each of three pairs of terminals on fiber #6 (3 separate larvae). SD shown. **G**, Estimates of the average number of AZs (with or without T-bars) for the different terminal types. Estimates were made by combining data in D (N=6) and F (N=3). SEM shown in G. Error bars in G calculated according to propagation of uncertainty theory.

Figure 2. **Type-Is terminals release more neurotransmitter than type-Ib during a single action potential. A**, Cross-section of muscle fibers and their innervating MNs. MNs are color-coded. MNSNb/d-II and MN12-III and other terminals of MNSNb/d-Is (*) are omitted for clarity. The current-clamp recording configuration is shown with micropipette (electrode) tips in adjacent muscle fibers (A). Two-electrode voltage clamp (TEVC) was achieved after withdrawing a micropipette from muscle 13 and placing it in muscle 6 (grey outline) (data in B-E). **B**, Excitatory Junction Currents (EJCs) recorded in muscle 6 in two separate preparations, and miniature EJCs (mEJCs) from one of those preparations. **C**, Average EJC amplitudes (Is: N=17; Ib: N=15; Student's t-tests, *$P<0.01$). Miniature EJCs (mEJCs) recorded from the two terminals at the same time as the EJCs had similar amplitudes (Is: 0.919±0.040 nA, N=17; Ib: 0.916±0.046 nA, N=15, SEM, $P=0.96$). **D**, Quantal content shown after correcting mEJC amplitudes using scaling factors (see **Experimental Procedures** for explanation). **E**, Estimates of average release site probability (P_{AZ}), calculated by dividing corrected quantal content (QC, Is: N=17; Ib: N=15) (D and Table S1) by total AZ number (N_{AZ}, N=6, Figure 1G) for each

terminal type. Error bars show SEM in C, D and E. Error bars calculated according to propagation of uncertainty theory in E. All recordings performed in TEVC in 2mM $[Ca^{2+}]_o$ 15mM $[Mg^{2+}]_o$ HL6.

Figure 3. Type-Is terminals display larger $[Ca^{2+}]_i$ transients during single action potentials, but less total Ca^{2+} enters these terminals. A, Inverted grayscale images of type-Ib and -Is bouton terminals filled with AF647-dextran (top; average of 20 frames collected at 20 fps) and of Oregon-Green BAPTA-1 (OGB-1) dextran (middle & bottom; average of 10 frames at 100 fps). The middle and bottom images show an average of OGB-1 fluorescence in the 100 ms period prior, and subsequent to, each of 10 stimuli delivered at 1 Hz, respectively. **B**, Average $[Ca^{2+}]_i$ for a single AP, calculated from 10 synchronized stimuli, estimated from the ratio of OGB-1 to AF647 fluorescence calibrated relative to $[Ca^{2+}]_i$ (see **Experimental Procedures**). **C**, Plots of the average maximal change in $[Ca^{2+}]_i$ ($\Delta[Ca^{2+}]_{AP}$) for 12 different pairs of terminals filled with OGB-1 and AF647 on muscle 6. Averages shown as open symbols (*, $P<0.01$). **D**, Plots of the change in total $[Ca^{2+}]_i$ (free plus bound), calculated using equation 5 : $\Delta[Ca^{2+}]_{total} = \Delta[Ca^{2+}]_{AP} \times (1 + K_S + K'_B)$, (*, $P<0.05$). **E**, A plot of the average number of Ca^{2+} ions that enter each terminal in response to a single AP (calculated using equation 4). Paired Student's t-tests were conducted in C and D, and SEM is shown. Error bars calculated according to propagation of uncertainty theory in E.

Figure 4. In response to a single action potential, type-Is terminals spend less ATP to release more glutamate. A, Pie chart representations of relative ATP demands for glutamate release and recycling [equation 3 (E_{Glu})], Ca^{2+} extrusion [equation 6 (E_{Ca2+})], and Na^+ extrusion [equation 8 (E_{Na+})] for each terminal type. The area of each sector is proportional to the number of ATP molecules used for each activity (**Table S1**). **B**, Plot of the average number of glutamate molecules released from each terminal type (Glu), adjacent to a stacked bar plot of the number of ATP molecules required for each activity (E_{Glu}, E_{Ca2+} and E_{Na+}). **C**, A plot of the energy efficiency of both terminals calculated using equation 11. Error bars in B-C calculated according to propagation of uncertainty theory.

Figure 5. Output plots from the analytical model (Appendix I) that explores the influences on presynaptic energy efficiency during a single action potential (AP). A, Simulation of the influence of changes in the magnitude of each parameter that contributes to P_{AZ} [Ca^{2+} entry per AZ (Ca^{2+}/AZ), sensitivity (S) and cooperativity (n_H)] on P_{AZ} itself. Type-Is and -Ib terminals are labeled in red and green, respectively. **B**, Simulation of the influence of changes in parameters that contribute to P_{AZ} on the amount of glutamate released by each terminal. **C**, Simulation of the influence of parameters that contribute to P_{AZ} on the energy efficiency of each terminal. **D**, Simulation of the

influence of P_{AZ} (magnitude adjusted by changing Ca^{2+} entry per AZ alone) on the energy efficiency of each terminal. **Inset**, Plots duplicated from B, showing that maximum efficiency does not occur until high on the sigmoid curves describing the dependence of glutamate release on Ca^{2+} entry per AZ, that part of the curves synonymous with high P_{AZ}. In each plot, curves were normalized to physiological levels along the abscissa (a nominal range of 0.2 to 5), by dividing by the physiological value of the dependent (ordinate) variable.

Figure 6. **Motor neurons innervating muscle fiber 6 both fire and depress at different rates. A**, Cross section of muscle fibers, their innervating MNs, and the current clamp recording configuration used to record EJPs during fictive locomotion. **B**, Sample trace of EJPs recorded in muscle fiber #6 in 0.8mM $[Ca^{2+}]_o$, while a separate electrode recorded simultaneously in muscle 13 (trace not shown) enabling identification of the MNs contributing EJPs – in this case all were from MN6/7-Ib. **C**, Profiles of EJCs recorded in TEVC in muscle 6 in separate preparations evoked through impulses delivered to the segment nerve in 2 mM $[Ca^{2+}]_o$. EJCs in each trace represent the current that flows across the plasmamembrane of muscle 6 when release is evoked exclusively from a MNSNb/d-Is (red) or MN6/7-Ib terminal (green). **D**, EJC profile summary; each symbol represents the average amplitude of EJCs for ≥6 preparations. EJC amplitude is measured as vertical displacement from the baseline immediately before each event. SD shown. **E**, Plot of the average number of glutamate molecules released in response to an AP, calculated from EJCs depressed to mid-train levels (Glu_{bursts}). **F**, Plot of the average number of glutamate molecules released per unit time (s) calculated from mid-train QC and the endogenous firing frequency (EFR) of each terminal type. Error bars in E and F calculated according to propagation of uncertainty theory. **G**, Pie chart representations of relative ATP demands / s for glutamate release and recycling, Ca^{2+} extrusion, and Na^+ extrusion for each terminal type when firing at their endogenous firing frequencies. * indicates abbreviations of $E_{Glu\text{-}bursts}$ / s, $E_{Ca2+\text{-}bursts}$ / s and $E_{Na+\text{-}bursts}$ / s, as E_{Glu^*}, E_{Ca2+^*} and E_{Na+^*} respectively. Total pie chart areas are proportional to $E_{total\text{-}bursts}$ / s.

Figure 7. **Low-efficiency type-Ib terminals fire longest during fictive locomotion. A**, An activity plot for both terminal types on muscle fiber #6, collected simultaneously; GCaMP5 fluorescence intensity is proportional to the most recent instantaneous firing frequency. GCaMP5 fluorescence divided by the fluorescence of co-expressed DsRed, and the ratio for each terminal normalized between 0 (rest) and 1 (maximum). DsRed is insensitive to physiological ranges of Ca^{2+} and pH. **B**, Plots of the proportion of time during which the activity trace exceeded 20% (dotted line) for each terminal in a pair (relative duty cycle, N=6). Averages shown as open circles. SD shown (*, $P<0.01$,

paired Student's t-test). **C**, Plot of the average number of glutamate molecules released per unit time (Glu / $s_{loco.}$) from each terminal type on muscle fiber #6 (see **Equation 12**). Estimates of the summed output from all terminals of the same axon are represented by the arrows. **D**, Plot of the number of ATP molecules required to support the activity calculated in C (including Ca^{2+} and Na^{+} handling) (E_{total} / $s_{loco.}$, see **Equation 13**), calculated to mimic presynaptic energy demands during body wall peristalsis in a freely moving animal. Estimates of the summed ATP demands of all terminals are represented by the arrows. **E**, Pie chart representations of the relative ATP demands per unit time (s) for glutamate release and recycling, Ca^{2+} and Na^{+} extrusion for both terminal types. Estimates of the summed ATP demands of all terminals of each MN are represented by the areas within the dashed circumferences. Error bars in C and D calculated according to propagation of uncertainty theory.

Experimental Procedures

Details on all Experimental Procedures can be found in Supplemental Experimental Procedures.

Supplemental Information

Supplemental Information includes Supplemental Experimental Procedures, five figures, two tables and an appendix.

Appendix I

An analytical model that simulates the influence of aspects of presynaptic morphology and function on presynaptic energy efficiency.

Part A: The relationship between P_{AZ} and Ca^{2+} influx per active zone (Ca)

P_{AZ} is defined as the average likelihood of a single quantum of neurotransmitter being released per active zone (AZ) in response to a presynaptic action potential:

$$\mathrm{P_{AZ}} = \frac{\mathrm{QC}}{\mathrm{N_{AZ}}} \qquad (\mathrm{A}.1)$$

where QC = total number of synaptic vesicles (SVs) exocytosed;

N_{AZ} = total number of AZs

Numerous studies have demonstrated that the dependence of neurotransmitter release on Ca^{2+} influx can be described by the Hill equation. The relationship between QC and Ca is described as the following equation:

$$\mathrm{QC} = \frac{\mathrm{N_{AZ}}}{1 + \mathrm{S^{-1}} \times \mathrm{Ca^{-n_H}}} \qquad (\mathrm{A}.2)$$

where S is the sensitivity to release neurotransmitter and n_H is the Hill coefficient [15, 36].

Combining equations (A.1) and (A.2), yields:

$$\mathrm{P_{AZ}} = \frac{1}{1 + \mathrm{S^{-1}} \times \mathrm{Ca^{-n_H}}} \qquad (\mathrm{A}.3)$$

From equation (A.3), it is evident that P_{AZ} is a compound parameter, determined by Ca, S and n_H, but independent of N_{AZ}. Plotting P_{AZ} against Ca, S or n_H (**Figure 5A**), shows that greater Ca^{2+} influx, S or n_H gives rise to higher P_{AZ}. For both terminals, physiological values of n_H were fixed at 3.

***Part B**: The relationship between Ca, and the relationship between P_{AZ}, and energy efficiency: a model of presynaptic energetics.*

Presynaptic energy efficiency is defined here as:

$$\mathrm{E.E.} = \frac{\mathrm{Glu}}{\mathrm{E_{total}}} \tag{A.4}$$

$$\mathrm{Glu} = \mathrm{QC} \times \varepsilon \tag{A.5}$$

where E.E. represents energy efficiency; ε = number of glutamate molecules in a SV, and ε is proportional to SV volume.

Together with equation (A.2), the number of glutamate molecules released is seen as a function of Ca, S, N_{AZ}, vesicle size and n_H (**Figure 5B; Figure S4A**).

Initially, total energy demand can be approximated as the sum of the cost of SV release and recycling, and the cost on Ca^{2+} extrusion [17, 29]:

$$\mathrm{E_{total}} = \mathrm{E_{Glu}} + \mathrm{E_{Ca^{2+}}} \tag{A.6}$$

where $\mathrm{E_{Glu}}$ represents the cost of releasing glutamate, which combines the costs of loading SVs with glutamate and recycling SVs. $\mathrm{E_{Ca^{2+}}}$ represents the cost of Ca^{2+} extrusion.

As Na^+ entry also contributes to action potential propagation in the nerve terminal, it is necessary to involve the cost of Na^+ extrusion in the nerve terminal. Taken together, equation (A.6) is now rewritten as:

$$\mathrm{E_{total}} = \mathrm{E_{Glu}} + \mathrm{E_{Ca^{2+}}} + \mathrm{E_{Na^{+}}} \tag{A.7}$$

where $\mathrm{E_{Na^{+}}}$ is the cost of the Na^+ load.

Each term in equation (A.7) is dealt with separately below.

$\mathrm{E_{Glu}}$ is calculated as the product of the number of SVs released (QC) and the cost per SV (ATP_{SV}):

$$\mathrm{E_{Glu}} = \mathrm{QC} \times \mathrm{ATP_{SV}} = \mathrm{QC} \times (\beta + \varepsilon \times \theta) \tag{A.8}$$

where β = number of ATP molecules spent to recycle a SV;

ε = number of glutamate molecules in a SV, proportional to SV size;

θ = number of ATP molecules needed to load a glutamate molecule

β = 410.5 and θ = 2.67 [29]. For the following simulation, these parameters are treated as constants while SV size changes along with Ca, N_{AZ}, S and n_H.

$\mathrm{E_{Ca^{2+}}}$ is calculated as the product of the total number of Ca^{2+} ions that enter the terminal (Ca_{total}, the same number that must be extruded) and the cost to extrude each Ca^{2+} (1 ATP molecule):

$$E_{Ca^{2+}} = Ca_{total} \times ATP_{Ca^{2+}} = Ca \times N_{AZ} \times 1\ ATP \quad (A.9)$$

Therefore, $E_{Ca^{2+}}$ is a function of Ca and N_{AZ}.

Similarly, E_{Na^+} is calculated as:

$$E_{Na^+} = Na_{total} \times \frac{1}{3} \times 1\ ATP \quad (A.10)$$

Na_{total} (Na^+ load) can be calculated using the following formula:

$$Na_{total} = C \times V \times O \quad (A.11)$$

where C represents the capacitance and can be calculated as the product of capacitance per surface area ($C_m = 1\ \mu F/\mu m^2$) and surface area of the terminal; V represents the voltage change of an AP; O represents overlap factor.

We measured the surface area of type-Ib and type-Is terminals (**Table S1**). The overlap factor refers to the ratio of the total integrated Na^+ current during the action potential to the minimum charge transfer necessary for action potential depolarization [32]. The overlap factor for honeybee neurons is 3.05 [34] and we assume that *Drosophila* nerve terminals have the same overlap factor. Taken together, we find that, under physiological conditions, E_{Na^+} for type-Ib terminals is 3.60 x 10^6 ATP molecules whileE_{Na^+} for type-Is nerve terminals is 1.48 x 10^6 molecules.

Simulating the effect of changing variables in equation (A.11), it is clear that [like total Ca^{2+} influx (**Figure S4B**)] the Na^+ load changes linearly with alterations in these parameters (**Figure S4C**). For subsequent analysis it is assumed that E_{Na^+} is independent of other parameters such as Ca, S, N_{AZ}, vesicle size and n_H. In other words, partial derivatives of variables such as Ca, E_{Na^+} will be constant.

Combining equations (A.5), (A.7), (A.8), (A.9) and (A.10) yields:

$$E.E. = \frac{QC \times \varepsilon}{QC \times (\beta + \varepsilon \times \theta) + Ca \times N_{AZ} \times ATP_{Ca^{2+}} + E_{Na^+}} \quad (A.12)$$

Based on equation (A.12), we can conclude that energy efficiency is a function of Ca as well as other parameters such as S, N_{AZ}, vesicle size and n_H (**Figure 5C; Figure S4D**). Parameters such as surface area and capacitance per surface area also affect energy efficiency through increase of E_{Na^+} [equation (A.11)], but unlike parameters discussed above, such parameters should be as small as possible to reduce the total energy demand. In other words, when E_{Na^+} is negligible, it is beneficial for increasing energy efficiency of a nerve terminal.

Furthermore, based on equations (A.1) and (A.3), equation (A.12) can be rewritten as:

$$\mathrm{E.E.} = \frac{\mathrm{P_{AZ}} \times \varepsilon}{\mathrm{P_{AZ}} \times (\beta + \varepsilon \times \theta) + ((\frac{1}{\mathrm{P_{AZ}}} - 1) \times \mathrm{S})^{\mathrm{n_H}} \times \mathrm{ATP_{Ca^{2+}}} + \frac{\mathrm{E_{Na^+}}}{\mathrm{N_{AZ}}}} \quad (\mathrm{A.13})$$

From the simulation data (**Figure 5D**), maximal energy efficiency is achieved when P_{AZ} is 0.76 in type-Is nerve terminals (physiological P_{AZ} in Is nerve terminals is 0.33); P_{AZ} is 0.73 in type-Ib nerve terminals (physiological P_{AZ} in Ib nerve terminals is 0.11). Therefore, the simulation indicates that a relatively high P_{AZ} confers high energy efficiency.

Part C, *Proof: Optimization of energy efficiency drives towards high P_{AZ}*

Ca is a unique variable since it is subject to changes within milliseconds [52]. In addition, the bell shaped plot of energy efficiency versus Ca is unique relative to the simulated dependency on other parameters in Figure **5C**. For these reasons we elaborated our model to determine whether a relatively high P_{AZ} is required for maximization of energy efficiency where Ca is the only independent variable.

Taking the derivative of equation (A.12) where Ca is the only independent variable (partial derivative):

$$\frac{\mathrm{d(E.E.)}}{\mathrm{d(Ca)}} = -\left(\mathrm{N_{AZ}} \times \mathrm{ATP_{Ca^{2+}}} \times \frac{1}{\mathrm{QC}} - \mathrm{N_{AZ}} \times \mathrm{ATP_{Ca^{2+}}} \times \frac{\mathrm{Ca}}{\mathrm{QC^2}} \frac{\mathrm{d(QC)}}{\mathrm{d(Ca)}} - \mathrm{E_{Na^+}} \times \frac{1}{\mathrm{QC^2}} \frac{\mathrm{d(QC)}}{\mathrm{d(Ca)}}\right) \times \frac{\varepsilon}{(\beta + \varepsilon \times \theta + \mathrm{Ca} \times \mathrm{N_{AZ}} \times \mathrm{ATP_{Ca^{2+}}} \div \mathrm{QC} + \mathrm{E_{Na^+}} \div \mathrm{QC})^2} \quad (\mathrm{A.14})$$

When $\frac{\mathrm{d(E.E)}}{\mathrm{d(Ca)}} = 0$, energy efficiency could be maximal, which is :

$$\frac{\mathrm{d(QC)}}{\mathrm{d(Ca)}} = \frac{\mathrm{QC}}{\mathrm{Ca} + \frac{\mathrm{E_{Na^+}}}{\mathrm{N_{AZ}} \times \mathrm{ATP_{Ca^{2+}}}}} \quad (\mathrm{A.15})$$

A general solution for equation (A.15) is:

$$\mathrm{QC} = \varphi \times \mathrm{Ca} + \omega \tag{A.16}$$

with φ and ω as non-zero constants.

The range of Ca for optimal energy efficiency can be further refined as follows.

From equation (A.2), if $Z = 1 + S^{-1} \times Ca^{-n_H}$ then:

$$\frac{\mathrm{d(QC)}}{\mathrm{d(Ca)}} = \mathrm{N_{AZ}} \times \left(\frac{-\mathrm{Z'}}{\mathrm{Z^2}}\right) = -\frac{\mathrm{N_{AZ}}}{\mathrm{Z^2}} \times \mathrm{S^{-1}} \times (-\mathrm{n_H}) \times \mathrm{Ca^{-n_H-1}}$$
$$= \frac{\mathrm{N_{AZ}} \times \mathrm{S^{-1}} \times \mathrm{n_H}}{\mathrm{Z^2}} \times \mathrm{Ca^{-n_H-1}} \tag{A.17}$$

Combining equation (A.17) with equations (A.2) and (A.14), we get:

$$\mathrm{S^{-1}} \times (\mathrm{n_H} - 1) \times \mathrm{Ca} + \mathrm{E_{Na^+}} \times \mathrm{S^{-1}} \times \mathrm{n_H} \div (\mathrm{N_{AZ}} \times 1\ \mathrm{ATP}) = \mathrm{Ca^{n_H+1}} \tag{A.18}$$

After rearranging equation (A.18);

$$\mathrm{Ca^{n_H+1}} - \mathrm{S^{-1}} \times (\mathrm{n_H} - 1) \times \mathrm{Ca} = \mathrm{E_{Na^+}} \times \mathrm{S^{-1}} \times \mathrm{n_H} \div (\mathrm{N_{AZ}} \times 1\ \mathrm{ATP})$$

As the term on the right must be a positive value;

$$\mathrm{Ca^{n_H+1}} - \mathrm{S^{-1}} \times (\mathrm{n_H} - 1) \times \mathrm{Ca} > 0$$

After rearranging:

$$\mathrm{Ca} > \left(\frac{\mathrm{n_H} - 1}{\mathrm{S}}\right)^{\left(\frac{1}{\mathrm{n_H}}\right)} \tag{A.19}$$

This indicates that Ca needs to exceed a certain value for optimal energy efficiency. According to equation (A.3), high Ca gives rise to high P_{AZ}. Similarly, optimization of energy efficiency requires high S and n_H (**Figure 5C**); and high S or n_H yields high P_{AZ} (**Figure 5A**). To conclude, a high P_{AZ} value

exceeding a certain value is required for maximization of energy efficiency. The actual value is determined as follows:

In a special case, if E_{Na^+} is negligible compared with $\mathrm{E_{Glu}}$ and $\mathrm{E_{Ca^{2+}}}$, then equation (18) can be rewritten as follows:

$$\mathrm{S^{-1} \times (n_H - 1) \times Ca = Ca^{n_H+1}} \qquad (A.20)$$

After rearranging:

$$\mathrm{Ca} = \left(\frac{\mathrm{n_H - 1}}{\mathrm{S}}\right)^{\left(\frac{1}{\mathrm{n_H}}\right)} \qquad (A.21)$$

Therefore, there is a single solution for Ca where energy efficiency is maximized, and from our data we determined the values to be: Is, 18,100 ions; Ib: 14,650 ions.

Combining equation (A.21) and equation (A.3), P_{AZ} can be calculated under conditions where $\mathrm{E_{Na^+}}$ is negligible, and energy efficiency is optimal:

$$\mathrm{P_{AZ}} = \frac{1}{1 + \mathrm{S^{-1} \times Ca^{-n_H}}} = \frac{1}{1 + \mathrm{S^{-1} \times \left(\left(\frac{n_H - 1}{S}\right)^{\left(\frac{1}{n_H}\right)}\right)^{-n_H}}} = \frac{1}{1 + \mathrm{S^{-1} \times \left(\frac{n_H - 1}{S}\right)^{-1}}} = \frac{\mathrm{n_H - 1}}{\mathrm{n_H}} \qquad (A.22)$$

As n_H = 3 in both type-Is and type-Ib nerve terminals, from equation (A.22), P_{AZ}=0.67. If $\mathrm{E_{Na^+}}$ is not negligible, efficiency maximization can only be reached when P_{AZ}>0.67, consistent with the plots in **figure 5D**.

Therefore, our analysis suggests that optimization of energy efficiency drives towards high P_{AZ}, a conclusion that should be generalizable to all presynaptic terminals where neurotransmitter release has a steep dependence on Ca^{2+} entry.

Author Contributions

Zhongmin.L. and G.T.M. designed experiments. Zhongmin.L., A.K.C., J.A.B., Zhiyuan.L., A.J.R., Y.Z. and G.T.M. performed experiments. Zhongmin.L., A.K.C., J.A.B., Zhiyuan.L., A.J.R., K.L.B., Y.Z., I.A.M. and G.T.M. performed analyses. Zhongmin.L., K.L.B. and G.T.M. wrote the manuscript. Zhongmin.L., A.K.C., J.A.B., Zhiyuan.L., A.J.R., K.L.B., I.A.M. and G.T.M. reviewed the manuscript. G.T.M. supervised and acquired funding.

Acknowledgements

Stocks obtained from the Bloomington Drosophila Stock Center (NIH P40OD018537). We are grateful for discussions with Drs. David Attwell and Stephen Meriney that improved our manuscript. The graphical abstract was assembled by Christopher Tepetitlan and Daniel Rico-Madrazo of the Florida Atlantic University Wilkes Honors College. GTM was supported by NIH NINDS award NS061914.

REFERENCES

1. Cowan, W.M., S©*dhof, T.C., Stevens, C.F., and Howard Hughes Medical Institute. (2001). Synapses, (Baltimore: Johns Hopkins University Press).
2. Varshney, L.R., Sjostrom, P.J., and Chklovskii, D.B. (2006). Optimal information storage in noisy synapses under resource constraints. Neuron *52*, 409-423.
3. Atwood, H.L., and Karunanithi, S. (2002). Diversification of synaptic strength: presynaptic elements. Nat Rev Neurosci *3*, 497-516.
4. Schneggenburger, R., Sakaba, T., and Neher, E. (2002). Vesicle pools and short-term synaptic depression: lessons from a large synapse. Trends Neurosci *25*, 206-212.
5. Harris, J.J., Jolivet, R., and Attwell, D. (2012). Synaptic energy use and supply. Neuron *75*, 762-777.
6. Levy, W.B., and Baxter, R.A. (2002). Energy-efficient neuronal computation via quantal synaptic failures. J Neurosci *22*, 4746-4755.
7. Jack, J.J., Redman, S.J., and Wong, K. (1981). The components of synaptic potentials evoked in cat spinal motoneurones by impulses in single group Ia afferents. J Physiol *321*, 65-96.
8. Walmsley, B., Edwards, F.R., and Tracey, D.J. (1988). Nonuniform release probabilities underlie quantal synaptic transmission at a mammalian excitatory central synapse. J Neurophysiol *60*, 889-908.
9. Lavidis, N.A., and Bennett, M.R. (1992). Probabilistic secretion of quanta from visualized sympathetic nerve varicosities in mouse vas deferens. J Physiol *454*, 9-26.
10. Hessler, N.A., Shirke, A.M., and Malinow, R. (1993). The probability of transmitter release at a mammalian central synapse. Nature *366*, 569-572.
11. Rosenmund, C., Clements, J.D., and Westbrook, G.L. (1993). Nonuniform probability of glutamate release at a hippocampal synapse. Science *262*, 754-757.
12. Murthy, V.N., Sejnowski, T.J., and Stevens, C.F. (1997). Heterogeneous release properties of visualized individual hippocampal synapses. Neuron *18*, 599-612.
13. Branco, T., and Staras, K. (2009). The probability of neurotransmitter release: variability and feedback control at single synapses. Nat Rev Neurosci *10*, 373-383.
14. Atwood, H.L., and Bittner, G.D. (1971). Matching of excitatory and inhibitory inputs to crustacean muscle fibers. J Neurophysiol *34*, 157-170.
15. Schneggenburger, R., and Neher, E. (2000). Intracellular calcium dependence of transmitter release rates at a fast central synapse. Nature *406*, 889-893.
16. Hall, C.N., Klein-Flugge, M.C., Howarth, C., and Attwell, D. (2012). Oxidative phosphorylation, not glycolysis, powers presynaptic and postsynaptic mechanisms underlying brain information processing. J Neurosci *32*, 8940-8951.
17. Liotta, A., Rosner, J., Huchzermeyer, C., Wojtowicz, A., Kann, O., Schmitz, D., Heinemann, U., and Kovacs, R. (2012). Energy demand of synaptic transmission at the hippocampal Schaffer-collateral synapse. J Cereb Blood Flow Metab *32*, 2076-2083.
18. Hoang, B., and Chiba, A. (2001). Single-cell analysis of Drosophila larval neuromuscular synapses. Dev Biol *229*, 55-70.
19. Halpern, M.E., Chiba, A., Johansen, J., and Keshishian, H. (1991). Growth cone behavior underlying the development of stereotypic synaptic connections in Drosophila embryos. J Neurosci *11*, 3227-3238.

20. Sink, H., and Whitington, P.M. (1991). Location and connectivity of abdominal motoneurons in the embryo and larva of Drosophila melanogaster. J Neurobiol *22*, 298-311.
21. Jan, L.Y., and Jan, Y.N. (1982). Antibodies to horseradish peroxidase as specific neuronal markers in Drosophila and in grasshopper embryos. Proc Natl Acad Sci U S A *79*, 2700-2704.
22. Kittel, R.J., Wichmann, C., Rasse, T.M., Fouquet, W., Schmidt, M., Schmid, A., Wagh, D.A., Pawlu, C., Kellner, R.R., Willig, K.I., et al. (2006). Bruchpilot promotes active zone assembly, Ca2+ channel clustering, and vesicle release. Science *312*, 1051-1054.
23. Guan, B., Hartmann, B., Kho, Y.H., Gorczyca, M., and Budnik, V. (1996). The Drosophila tumor suppressor gene, dlg, is involved in structural plasticity at a glutamatergic synapse. Curr Biol *6*, 695-706.
24. Karunanithi, S., Marin, L., Wong, K., and Atwood, H.L. (2002). Quantal size and variation determined by vesicle size in normal and mutant Drosophila glutamatergic synapses. J Neurosci *22*, 10267-10276.
25. Macleod, G.T., Hegstrom-Wojtowicz, M., Charlton, M.P., and Atwood, H.L. (2002). Fast calcium signals in Drosophila motor neuron terminals. J Neurophysiol *88*, 2659-2663.
26. Stewart, B.A., Atwood, H.L., Renger, J.J., Wang, J., and Wu, C.F. (1994). Improved stability of Drosophila larval neuromuscular preparations in haemolymph-like physiological solutions. J Comp Physiol A *175*, 179-191.
27. Leff, H.S., and Rex, A.F. (1990). Maxwell's demon : entropy, information, computing, (Princeton, N.J.: Princeton University Press).
28. Pawlu, C., DiAntonio, A., and Heckmann, M. (2004). Postfusional control of quantal current shape. Neuron *42*, 607-618.
29. Attwell, D., and Laughlin, S.B. (2001). An energy budget for signaling in the grey matter of the brain. J Cereb Blood Flow Metab *21*, 1133-1145.
30. Helmchen, F., Imoto, K., and Sakmann, B. (1996). Ca2+ buffering and action potential-evoked Ca2+ signaling in dendrites of pyramidal neurons. Biophys J *70*, 1069-1081.
31. Alle, H., Roth, A., and Geiger, J.R. (2009). Energy-efficient action potentials in hippocampal mossy fibers. Science *325*, 1405-1408.
32. Carter, B.C., and Bean, B.P. (2009). Sodium entry during action potentials of mammalian neurons: incomplete inactivation and reduced metabolic efficiency in fast-spiking neurons. Neuron *64*, 898-909.
33. Hodgkin, A.L., and Huxley, A.F. (1952). A quantitative description of membrane current and its application to conduction and excitation in nerve. J Physiol *117*, 500-544.
34. Sengupta, B., Stemmler, M., Laughlin, S.B., and Niven, J.E. (2010). Action potential energy efficiency varies among neuron types in vertebrates and invertebrates. PLoS Comput Biol *6*, e1000840.
35. Zielinski, S., and Portner, H.O. (1996). Energy metabolism and ATP free-energy change of the intertidal worm Sipunculus nudus below a critical temperature. J Comp Physiol B *166*, 492-500.
36. Heil, P., and Neubauer, H. (2010). Summing Across Different Active Zones can Explain the Quasi-Linear Ca-Dependencies of Exocytosis by Receptor Cells. Front Synaptic Neurosci *2*, 148.
37. Muller, M., and Davis, G.W. (2012). Transsynaptic control of presynaptic Ca(2)(+) influx achieves homeostatic potentiation of neurotransmitter release. Curr Biol *22*, 1102-1108.

38. Budnik, V., Zhong, Y., and Wu, C.F. (1990). Morphological plasticity of motor axons in Drosophila mutants with altered excitability. J Neurosci *10*, 3754-3768.
39. Chouhan, A.K., Zhang, J., Zinsmaier, K.E., and Macleod, G.T. (2010). Presynaptic mitochondria in functionally different motor neurons exhibit similar affinities for Ca2+ but exert little influence as Ca2+ buffers at nerve firing rates in situ. J Neurosci *30*, 1869-1881.
40. Klose, M.K., Chu, D., Xiao, C., Seroude, L., and Robertson, R.M. (2005). Heat shock-mediated thermoprotection of larval locomotion compromised by ubiquitous overexpression of Hsp70 in Drosophila melanogaster. J Neurophysiol *94*, 3563-3572.
41. Macleod, G.T., Marin, L., Charlton, M.P., and Atwood, H.L. (2004). Synaptic vesicles: test for a role in presynaptic calcium regulation. J Neurosci *24*, 2496-2505.
42. Hasenstaub, A., Otte, S., Callaway, E., and Sejnowski, T.J. (2010). Metabolic cost as a unifying principle governing neuronal biophysics. Proc Natl Acad Sci U S A *107*, 12329-12334.
43. Hesse, J., and Schreiber, S. (2015). Externalization of neuronal somata as an evolutionary strategy for energy economization. Curr Biol *25*, R324-325.
44. Attwell, D., and Gibb, A. (2005). Neuroenergetics and the kinetic design of excitatory synapses. Nat Rev Neurosci *6*, 841-849.
45. Niven, J.E., Anderson, J.C., and Laughlin, S.B. (2007). Fly photoreceptors demonstrate energy-information trade-offs in neural coding. PLoS Biol *5*, e116.
46. Niven, J.E., and Laughlin, S.B. (2008). Energy limitation as a selective pressure on the evolution of sensory systems. J Exp Biol *211*, 1792-1804.
47. Schreiber, S., Machens, C.K., Herz, A.V., and Laughlin, S.B. (2002). Energy-efficient coding with discrete stochastic events. Neural Comput *14*, 1323-1346.
48. Fioravante, D., and Regehr, W.G. (2011). Short-term forms of presynaptic plasticity. Curr Opin Neurobiol *21*, 269-274.
49. Koester, H.J., and Johnston, D. (2005). Target cell-dependent normalization of transmitter release at neocortical synapses. Science *308*, 863-866.
50. McLachlan, E.M. (1978). The statistics of transmitter release at chemical synapses. Int Rev Physiol *17*, 49-117.
51. Reyes, A., Lujan, R., Rozov, A., Burnashev, N., Somogyi, P., and Sakmann, B. (1998). Target-cell-specific facilitation and depression in neocortical circuits. Nat Neurosci *1*, 279-285.
52. Catterall, W.A., and Few, A.P. (2008). Calcium channel regulation and presynaptic plasticity. Neuron *59*, 882-901.

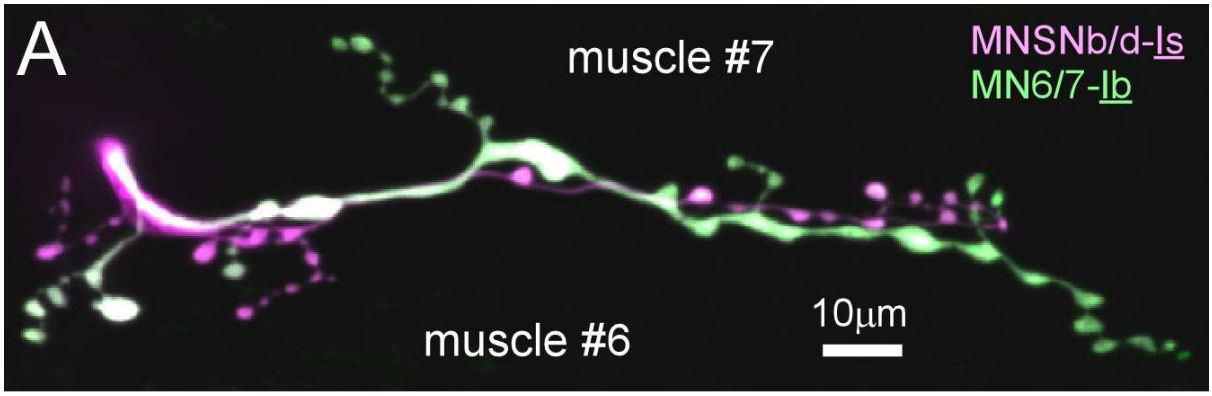
A
muscle #7
MNSNb/d-Is
MN6/7-Ib
muscle #6
10μm

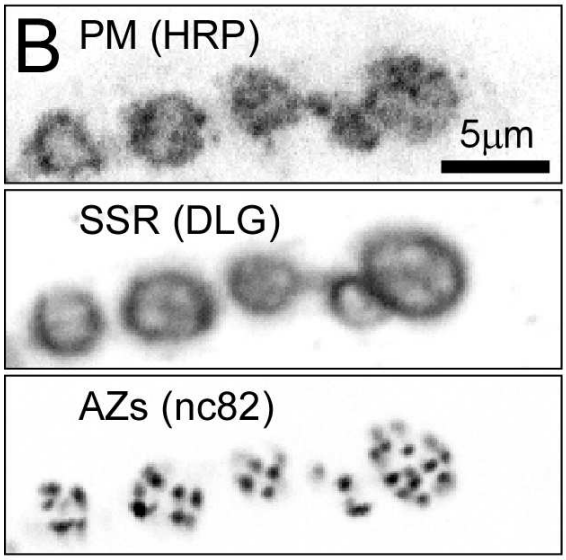
B
PM (HRP)
5μm
SSR (DLG)
AZs (nc82)

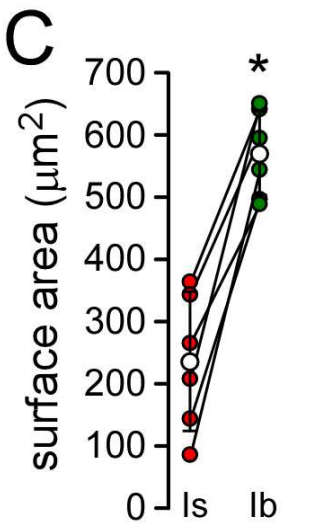
C
surface area (μm2)
700
600
500
400
300
200
100
0
Is
Ib
*

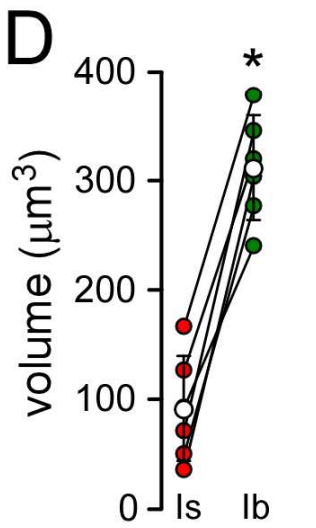
D
volume (μm3)
400
300
200
100
0
Is
Ib
*

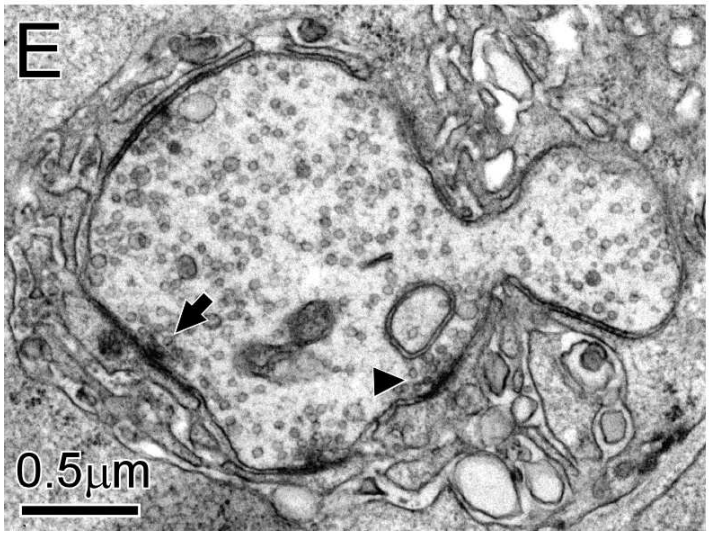
E
0.5μm

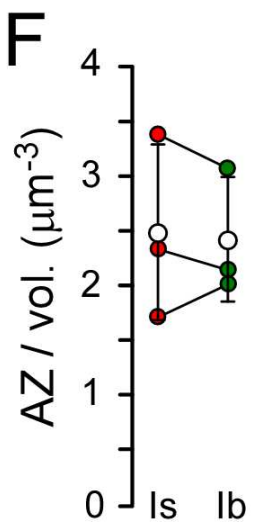
F
AZ / vol. (μm-3)
4
3
2
1
0
Is
Ib

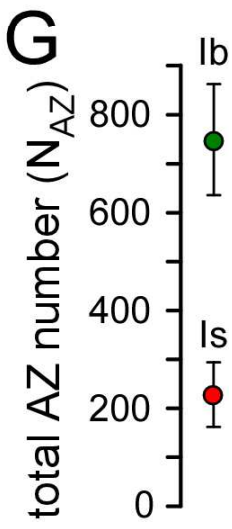
G
total AZ number (NAZ)
800
600
400
200
0
Ib
Is

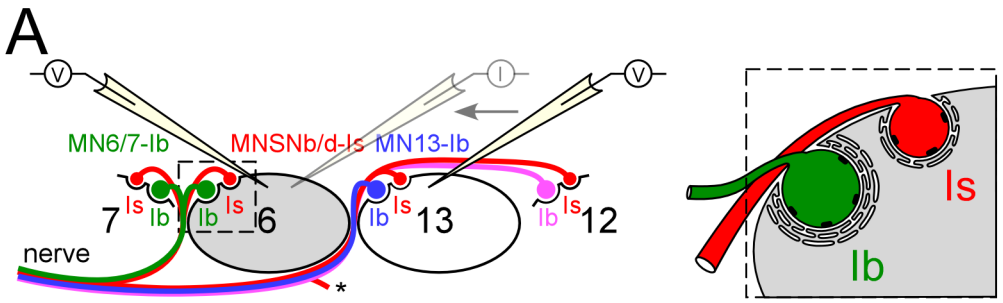
A
MN6/7-Ib
MNSNb/d-Is
MN13-Ib
7
6
13
12
Is
Ib
nerve
*
Is
Ib

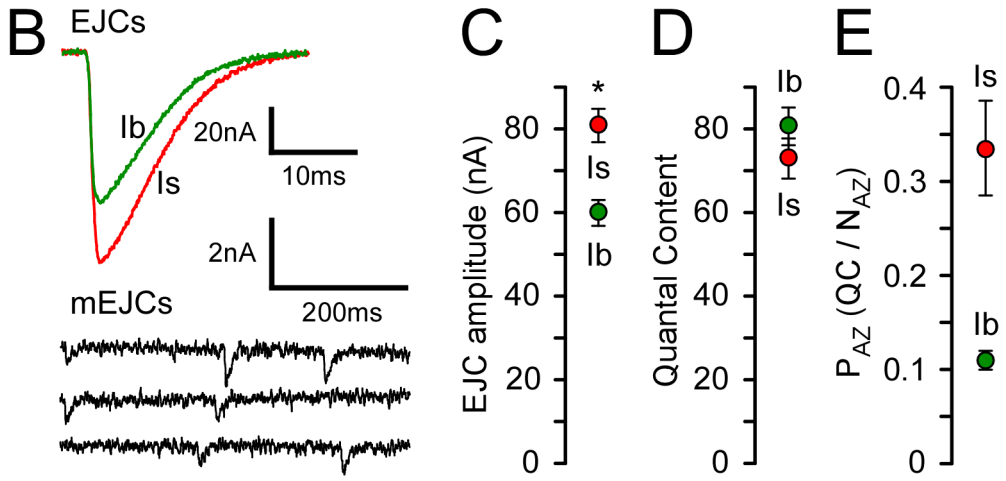
B
EJCs
Ib
Is
20nA
10ms
2nA
200ms
mEJCs
C
EJC amplitude (nA)
80
60
40
20
0
*
Is
Ib
D
Quantal Content
80
60
40
20
0
Ib
Is
E
P_{AZ} (QC / N_{AZ})
0.4
0.3
0.2
0.1
0
Is
Ib

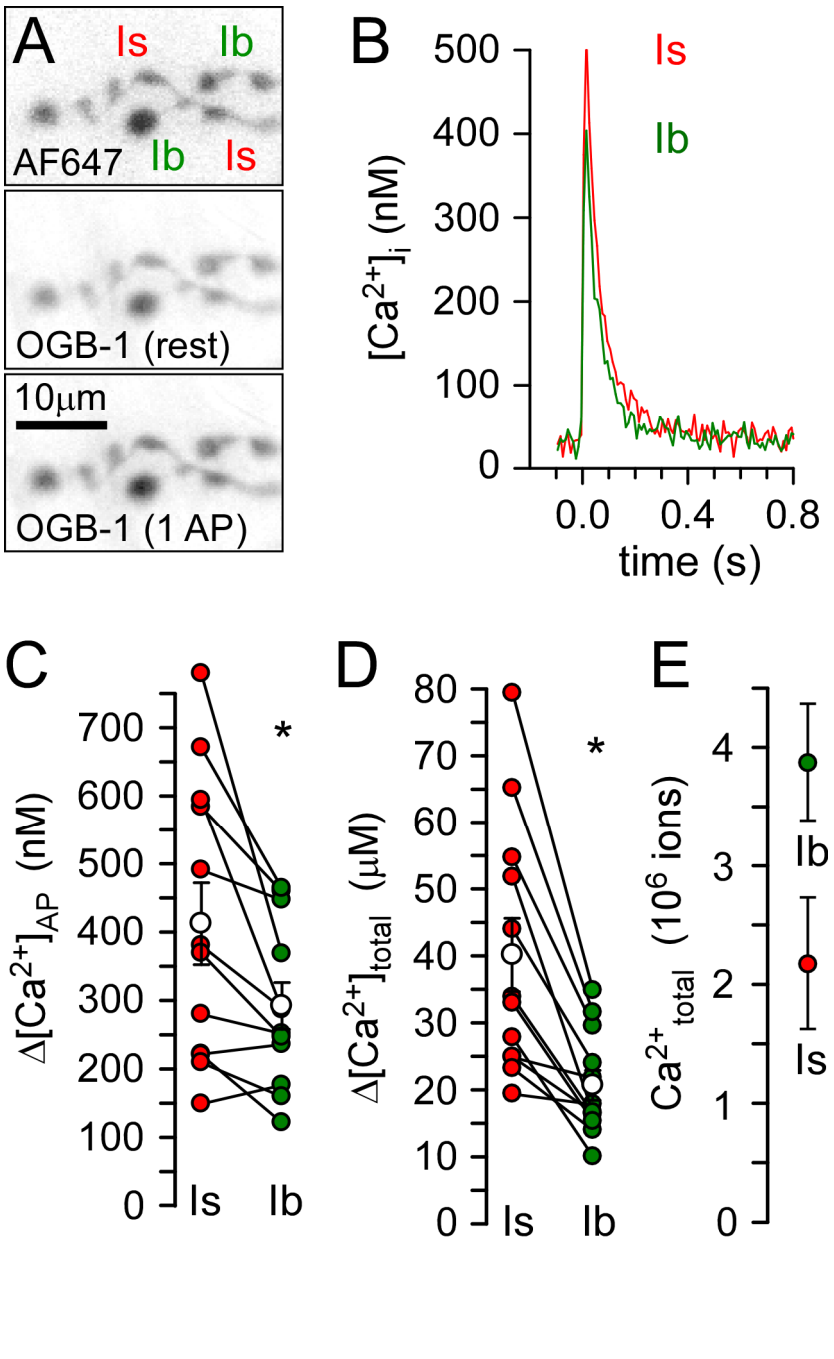
A
Is
Ib
AF647
Ib
Is
OGB-1 (rest)
10μm
OGB-1 (1 AP)
B
500
400
300
200
100
0
Is
Ib
[Ca2+]i (nM)
0.0
0.4
0.8
time (s)
C
700
600
500
400
300
200
100
0
*
Δ[Ca2+]AP (nM)
Is
Ib
D
80
70
60
50
40
30
20
10
0
*
Δ[Ca2+]total (μM)
Is
Ib
E
4
3
2
1
0
Ca2+ total (10^6 ions)
Ib
Is

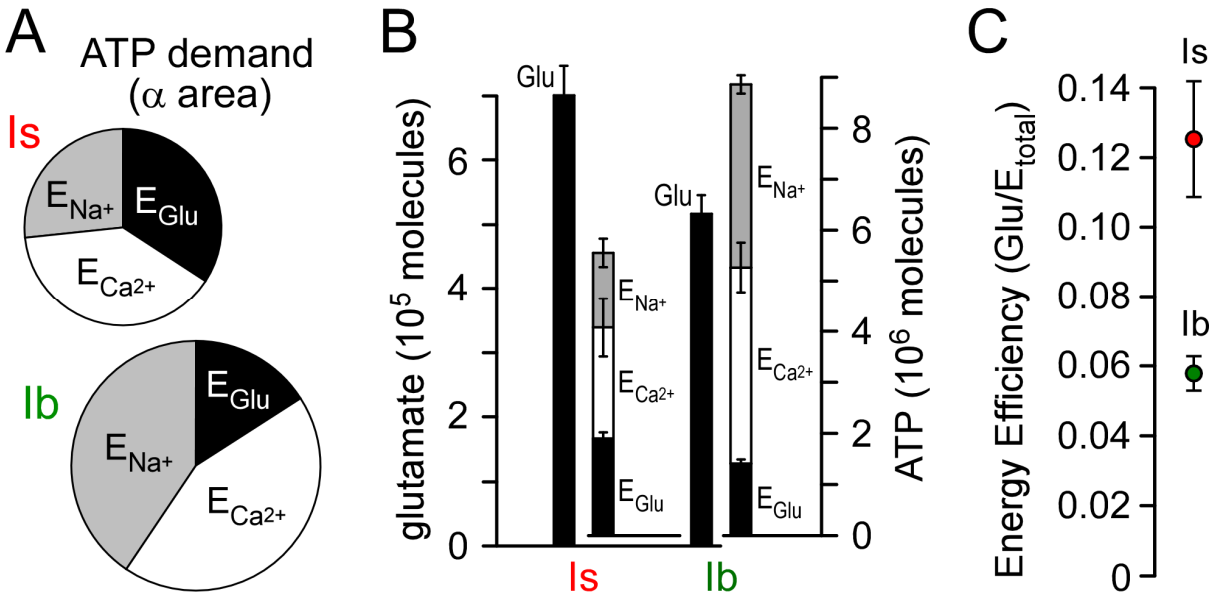
A
ATP demand
(α area)
Is
E Na+
E Glu
E Ca2+
Ib
E Glu
E Na+
E Ca2+
B
Glu
E Na+
E Ca2+
E Glu
Glu
E Na+
E Ca2+
E Glu
glutamate (10^5 molecules)
ATP (10^6 molecules)
0
2
4
6
0
2
4
6
8
Is
Ib
C
Energy Efficiency (Glu/E total)
0
0.02
0.04
0.06
0.08
0.10
0.12
0.14
Is
Ib

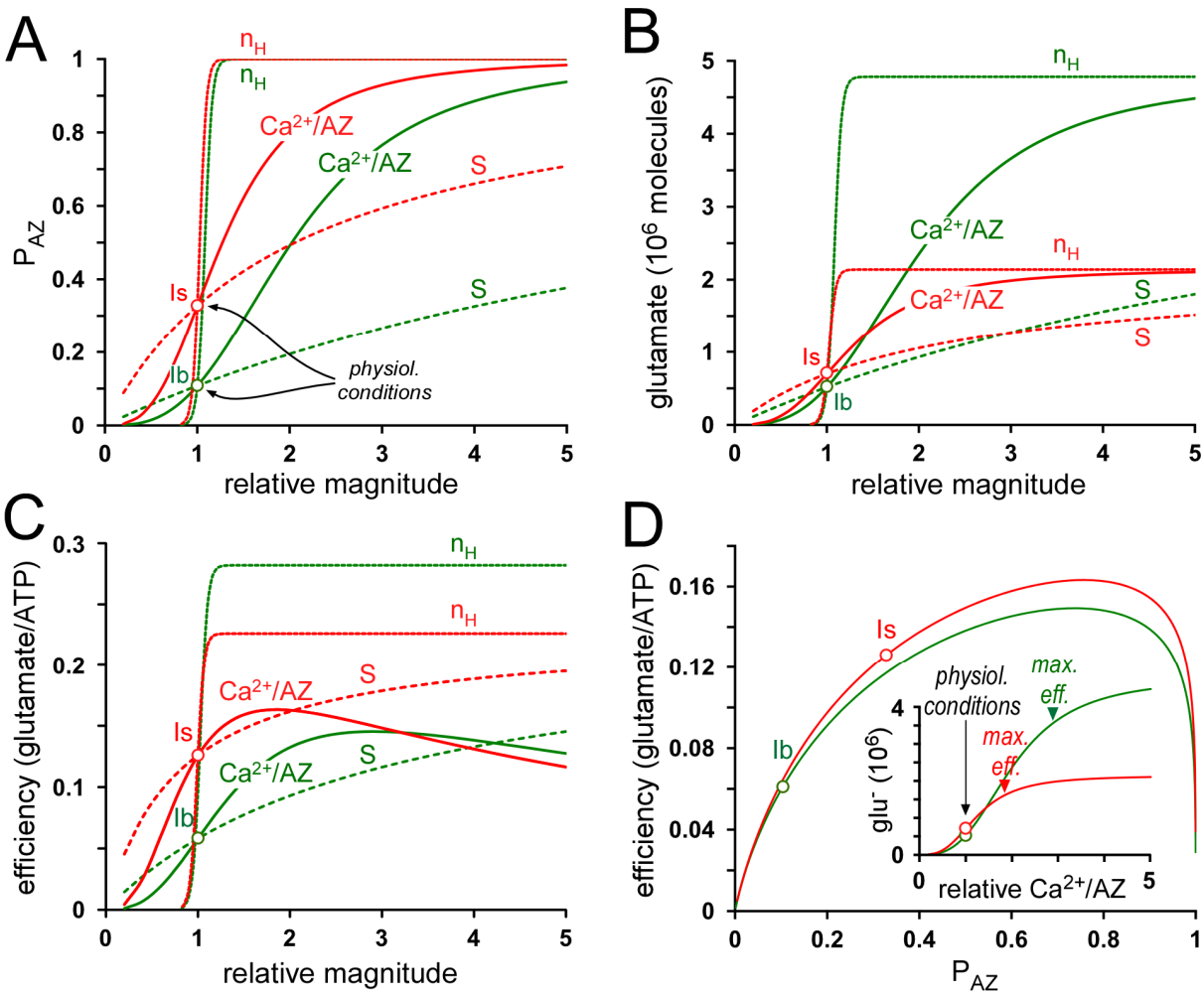
A
B
C
D
n_H
Ca^{2+}/AZ
S
Is
Ib
physiol. conditions
P_{AZ}
relative magnitude
glutamate (10^6 molecules)
efficiency (glutamate/ATP)
glu^- (10^6)
relative Ca^{2+}/AZ
max. eff.

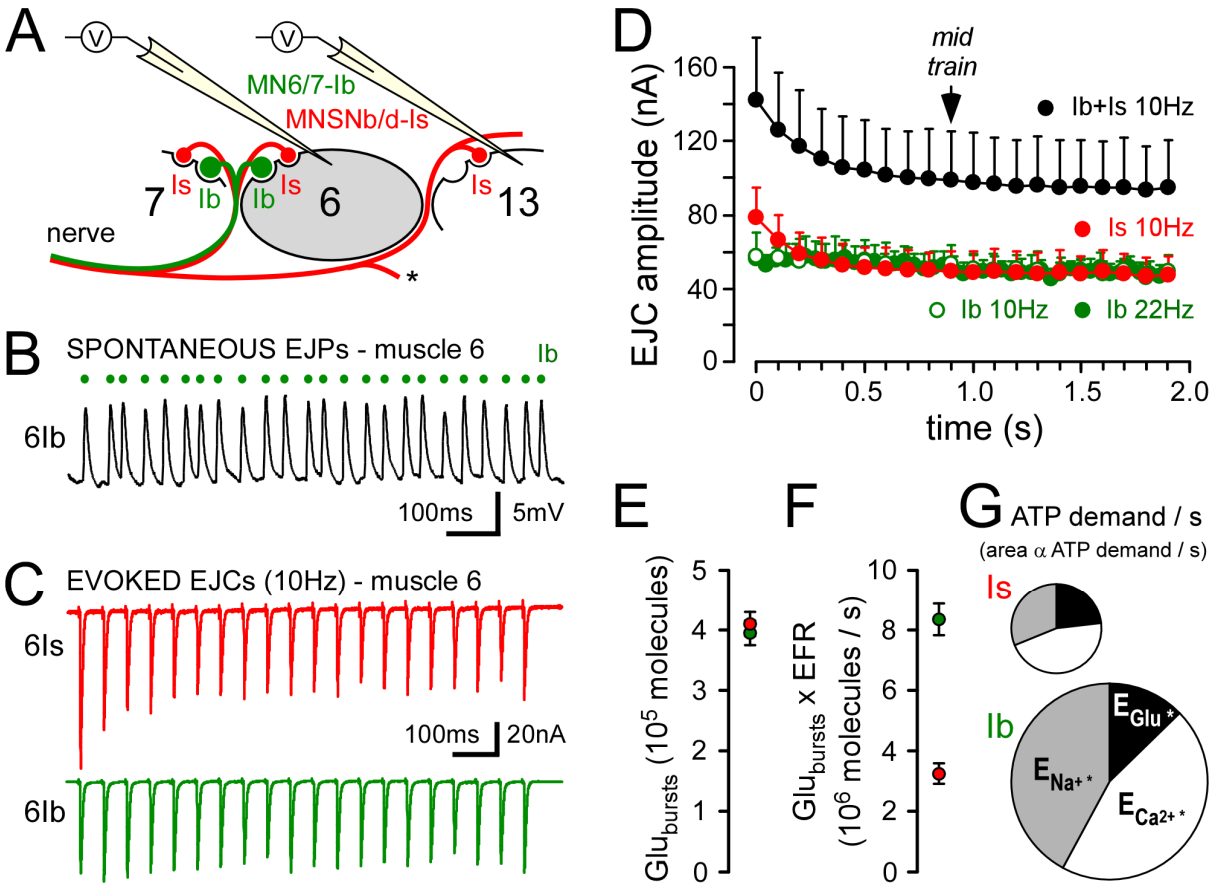
A
MN6/7-Ib
MNSNb/d-Is
7
Is
Ib
Ib
Is
6
Is
13
nerve
*
B
SPONTANEOUS EJPs - muscle 6
Ib
6Ib
100ms
5mV
C
EVOKED EJCs (10Hz) - muscle 6
6Is
100ms
20nA
6Ib
D
mid
train
Ib+Is 10Hz
Is 10Hz
Ib 10Hz
Ib 22Hz
EJC amplitude (nA)
160
120
80
40
0
0
0.5
1.0
1.5
2.0
time (s)
E
Glu_bursts (10^5 molecules)
5
4
3
2
1
0
F
Glu_bursts x EFR
(10^6 molecules / s)
10
8
6
4
2
0
G
ATP demand / s
(area α ATP demand / s)
Is
Ib
E_Glu*
E_Na+*
E_Ca2+*

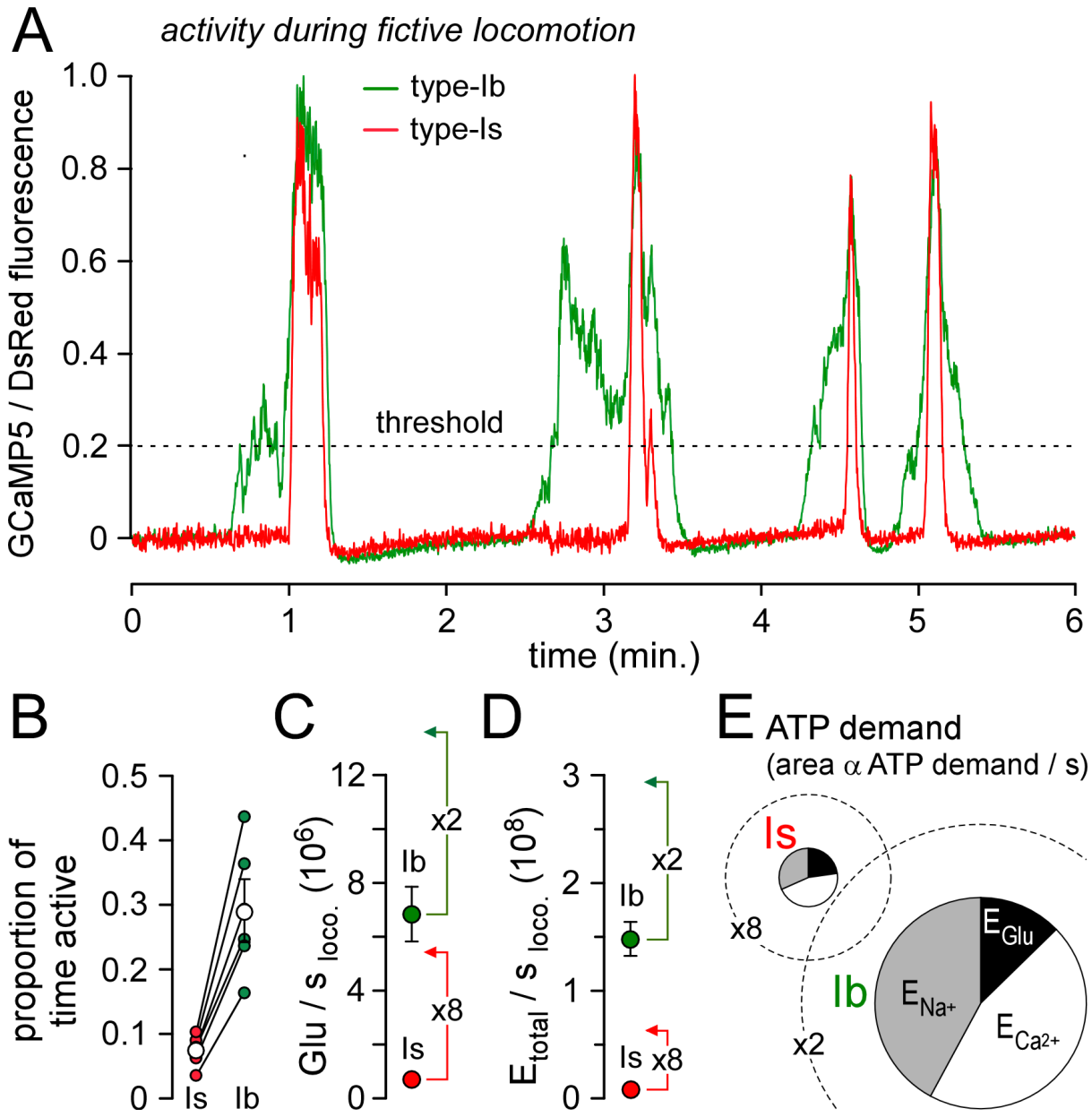
A
activity during fictive locomotion
type-Ib
type-Is
threshold
GCaMP5 / DsRed fluorescence
1.0
0.8
0.6
0.4
0.2
0
0
1
2
3
4
5
6
time (min.)
B
proportion of time active
0.5
0.4
0.3
0.2
0.1
0
Is
Ib
C
Glu / s loco. (10^6)
12
8
4
0
x2
Ib
x8
Is
D
E total / s loco. (10^8)
3
2
1
0
x2
Ib
Is
x8
E ATP demand
(area α ATP demand / s)
Is
x8
Ib
x2
E Glu
E Na+
E Ca2+

The NIHMS has received the file 'Supplemental Information - Lu.pdf' as supplementary data. The file will not appear in this PDF Receipt, but it will be linked to the web version of your manuscript.

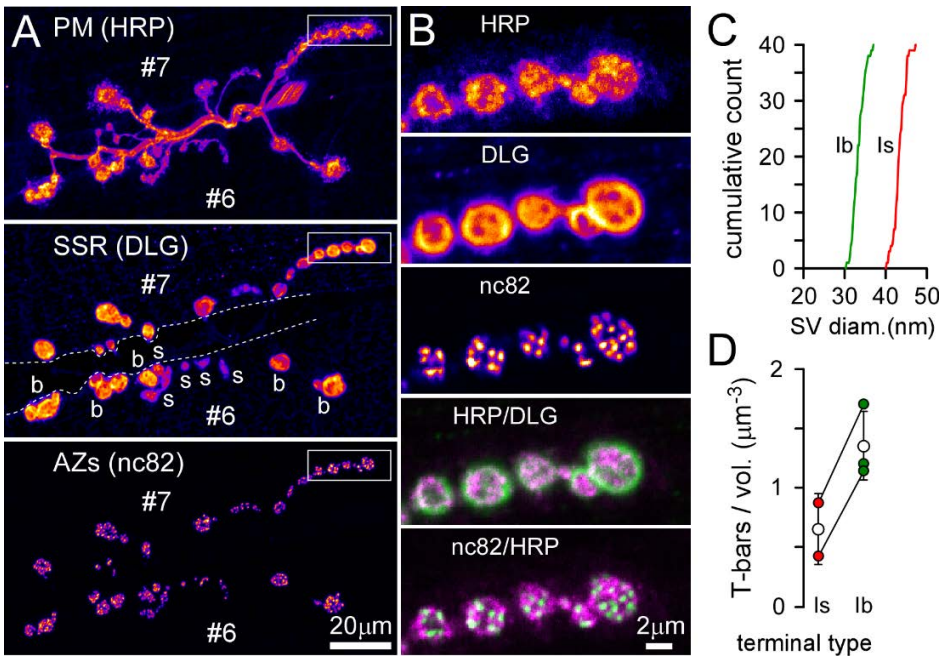

Figure S1. ***Two terminals types can be definitively identified on muscle #6 by both light and electron microscopic techniques*** (related to figure 1). Morphological quantification of type-Ib and type-Is terminals; synaptic vesicle outer diameters and T-bar active zones per unit volume (related to Figure 1). **A**, Immuno-fluorescence at neuromuscular junctions (NMJs) of two different motor neurons (MNSNb/d-Is and MN6/7-Ib) on muscle fibers #6 and #7. Antibody labelings reveal the neuronal plasmamembrane [PM, (Horseradish Peroxidase, HRP)], the postsynaptic sub-synaptic reticulum [SSR, (Discs Large, DLG)] and active zones [AZs, (Bruchpilot, nc82)]. A series of images was collected while advancing in steps through the entire depth of the terminals, then collapsed into a maximal intensity z-projection. Type-Ib boutons are distinguished by their larger size and dense DLG footprint. **B**, Labeling detail shown for the boxed regions in A (type-Ib boutons only). **C**, Cumulative distribution plots constructed from SV outer-diameter measurements for the purpose of unambiguous identification of terminal types (Ib vs Is) in electron micrographs. **D**, The number of AZs with T-bars per unit volume plotted for each of three pairs of terminals on muscle fiber #6 (3 separate larvae). The sample size was very small for one type-Is terminals (0.86 μm^3; whereas average volume was 5.2 μm^3 for the other two type-Is terminals, and 48.1 μm^3 for the three type-Ib terminals) and so data for the small type-Is sample (zero T-bars/vol.) are excluded from the average. SD is shown in D.

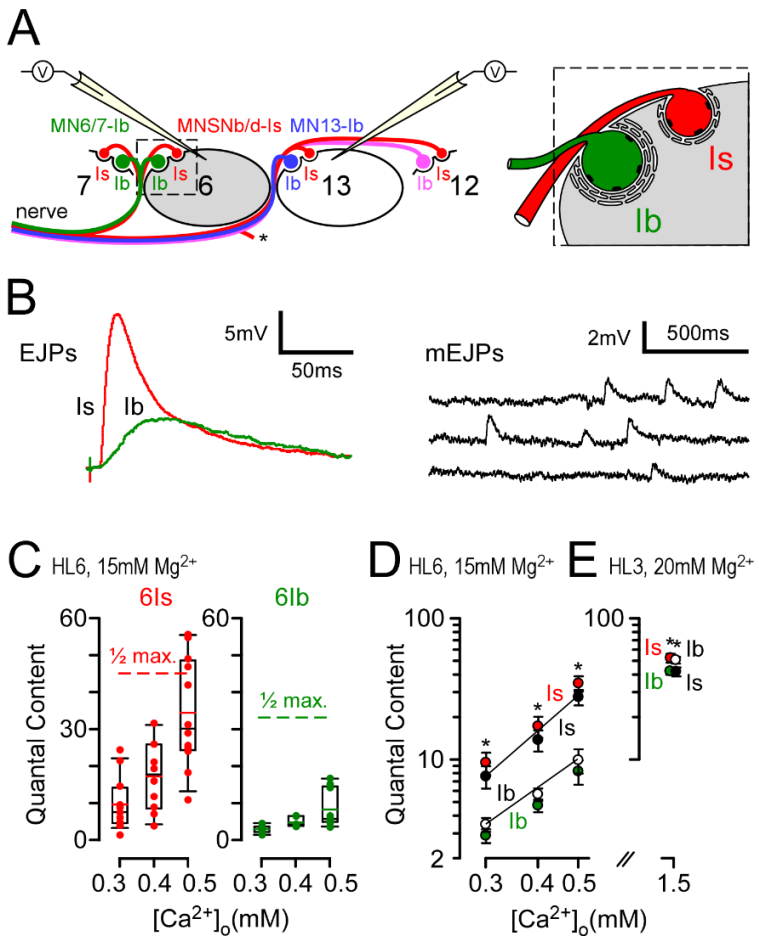

Figure S2. ***Type-Is terminals release more neurotransmitter than type-Ib terminals during a single action potential*** (related to figure 2). **A**, Cross-section of muscle fibers and their innervating MNs. The inset to the right shows detail of the boxed region on the left, emphasizing the larger sub-synaptic reticulum of the muscle beneath type-Ib boutons. MNs are color-coded. MNSNb/d-Is (red) and MN6/7-Ib (green) innervate muscle #6 with type-Is and -Ib boutons respectively. All data in this figure (B-E) were collected in current clamp mode and the recording micropipette (electrode) configuration is illustrated in A. **B**, Sample Excitatory Junction Potentials (EJPs) and miniature EJPs (mEJPs) recorded in muscle 6 of different preparations in which release could be evoked from either MN6/7-Ib alone or MNSNb/d-Is alone (see Experimental Procedures for the protocol). **C**, The Ca^{2+} dependence of release from type-Ib and -Is terminals; Quantal content (QC), was plotted according to convention (after correcting EJPs for nonlinear summation, but prior to correcting QC for different mEJP sizes) against $[Ca^{2+}]_o$ (N≥7 for each terminal type in each $[Ca^{2+}]_o$). Box-plots (25%-75%) show the mean (color), median (black) and whiskers (90%). "1/2 max " refers to half the QC values recorded at 2mM $[Ca^{2+}]_o$ in two-electrode voltage clamp (TEVC) (also prior to correction for different mEJC sizes; **Table S1**). **D**, Mean values from the plots in C were plotted on $\log_{10}$ axes and a straight line fit to the data using a least-squares algorithm. The power relationship between $[Ca^{2+}]_o$ and SV release was low for both terminal types (Is: 2.54; Ib: 2.07) but release from type-Is was significantly more sensitive to $[Ca^{2+}]_o$ [two-way ANOVA ($P<0.05$ overall), Tukey *post hoc* *$P<0.01$]. After correcting QC estimates for differences in mEJP size between terminals differences remained [black (Is) and white (Ib) symbols]. **E**, QC determined in another commonly used saline (Hemolymph-Like solution #3 (HL3), containing 20 mM $[Mg^{2+}]_o$ [S1]) with physiological $[Ca^{2+}]_o$ levels (1.5 mM). EJPs were recorded in current clamp mode and were larger at type-Is terminals (Is: 56.1±3.0 mV, N=9; Ib: 45.7±2.9 mV, N=21, Student's t-tests, *$P=0.06$), as were QC estimates (Is: 52.0±3.8, N=9; Ib: 42.0±2.3, N=21, *$P<0.05$). However, after adjustments for the larger mEJPs that originate from type-Is terminals, QC estimates were inverted relative to the EJP amplitudes (corrected QC: Is: 41.6±3.0; Ib: 50.4±2.7, *$P<0.05$). Error bars in D and E show SEM.

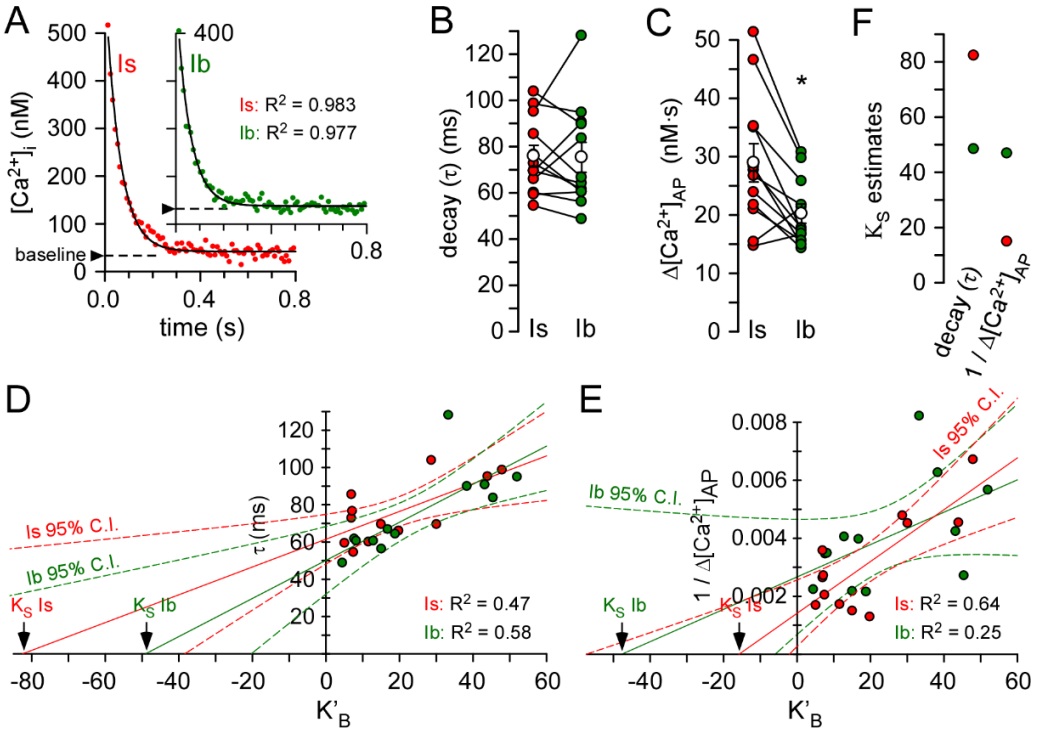

Figure S3. ***Type-Is terminals admit the least Ca^{2+} during an action potential, and the Ca^{2+} binding ratio (K_S) is higher in type-Is terminals than in type-Ib*** (related to figure 3). The two terminal types have a similar time course of $[Ca^{2+}]_i$ decay after an AP, but our best estimate of the Ca^{2+} binding ratio (K_S) indicates that K_S is higher in type-Is terminals (related to Figure 3). **A**, Single exponential curve fits (black lines) to the decay of $[Ca^{2+}]_i$ transients after single action potentials (APs). The same data as shown in Figure 3B. Each is the average of 10 events collected at 1Hz. The exponential was fit from 15 to 800ms after the nerve stimulus. The baseline was not defined for the curve-fit but in each case the fit approached to 10nM of the baseline within the fitted period. **B**, Plots of the average decay of $[Ca^{2+}]_i$ transients for 12 pairs of terminals. **C**, Plots of the integrals of the $[Ca^{2+}]_i$ transients, calculated as the product of τ and $\Delta[Ca^{2+}]_{AP}$ for each terminal (*, $P<0.05$). Averages shown as open symbols in B and C. All error bars show SEM. **D**, A plot of τ versus the incremental Ca^{2+}-binding ratio for OGB-1 (K'_B) for each of the two terminal types. Extrapolations of least-squares regressions to the abscissa give estimates of the endogenous Ca^{2+}-binding ratio (K_S) for each terminal. **E**, A plot of $1/\Delta[Ca^{2+}]_{AP}$ versus K'_B for each of the two terminal types. The dashed lines in D and E represent 95% confidence interval envelopes for straight line fits to the data from each terminal. **F**, A summary of the estimates of K_S generated from the two approaches from the same 12 pairs of terminals.

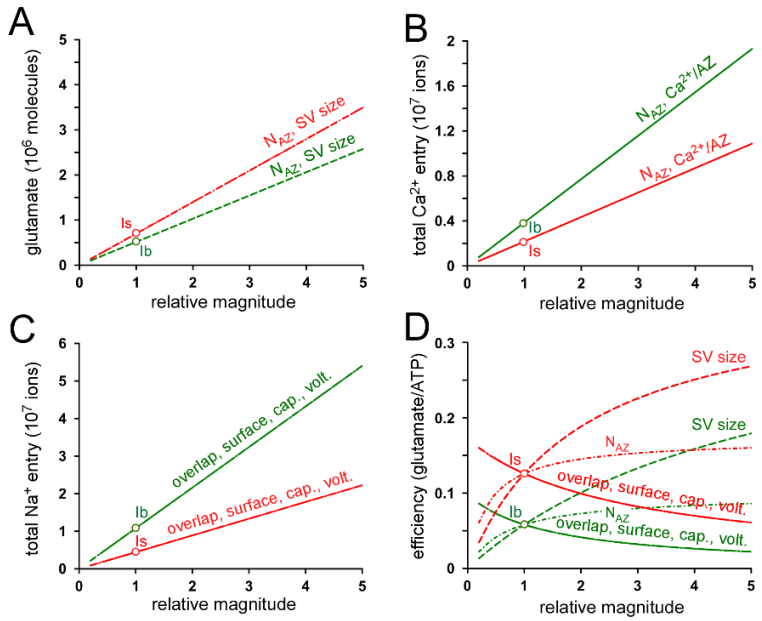

Figure S4. ***Output plots from the analytical model (Appendix I) that explores the influences on presynaptic energy efficiency during a single action potential*** (related to Figure 5). **A**, Simulation of the influence of changes in the magnitude of AZ number (N_{AZ}) and SV size on the amount of glutamate released by each terminal. Type-Is and -Ib terminals are labeled in red and green respectively. **B**, Simulation of the influence of changes in N_{AZ} and SV size on the amount of Ca^{2+} that enters each terminal. **C**, Simulation of the influence of action potential (AP) K^+ overlap with Na^+ (overlap), terminal surface area (surface), specific membrane capacitance (cap.) and AP voltage change (volt.) on the amount of Na^+ that enters each terminal. **D**, Simulation of the influence of the parameters introduced in A-C, on the energy efficiency of each terminal. In each plot, curves were normalized to physiological levels along the abscissa (a nominal range of 0.2 to 5), by dividing by the physiological value of the dependent (ordinate) variable.

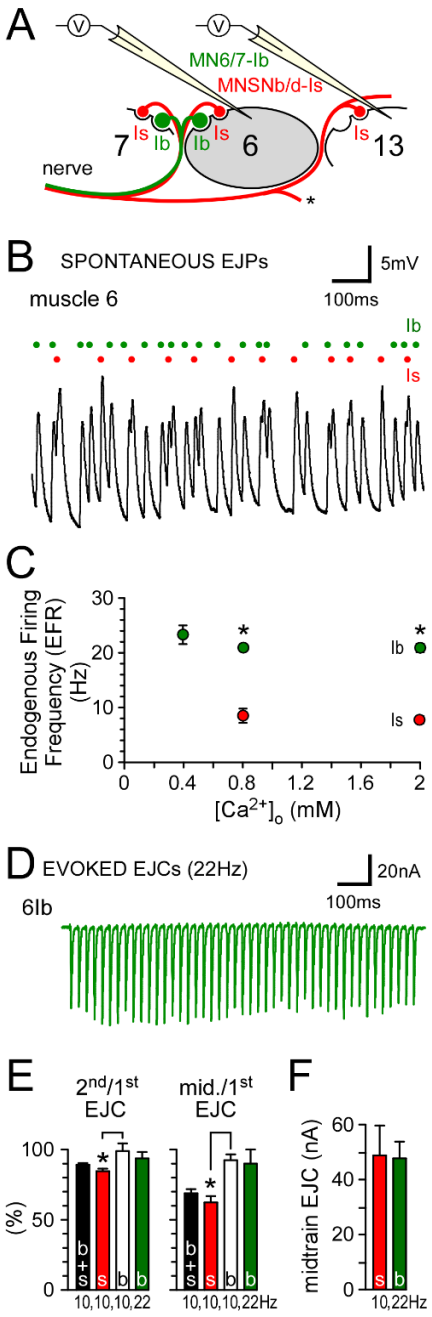

Figure S5. ***Motor neurons innervating muscle fiber 6 have endogenous firing frequencies (EFR) during motor patterns*** (related to Figure 6). **A**, Cross section of muscle fibers, their innervating MNs, and the current clamp recording configuration used to record EJPs during fictive locomotion. **B**, A sample trace of EJPs recorded in muscle fiber #6, while a trace from a micropipette recording simultaneously in muscle 13 (trace not shown) was used to identify the MNs contributing EJPs, according to the protocol described by [S2]. MN identity is indicated above each EJP in the traces. **C**, Average EJP frequency is represented for each contributing MN. $[Ca^{2+}]_o$ made no significant contribution to EJP frequency [two-way ANOVA ($P<0.05$ overall), Tukey *post hoc* *$P<0.001$]. The average EJP frequency across all $[Ca^{2+}]_o$ levels was calculated as Is: 8.1±0.7Hz (N=14); Ib: 21.1±0.6Hz (N=35); Student's t-test, $P<0.001$. Error bars show SEM. **D**, Profiles of EJCs recorded in two-electrode voltage clamp (TEVC) in muscle 6 in response to impulses delivered to segment nerve in 2mM $[Ca^{2+}]_o$. The trace represents current flow across the plasmamembrane of muscle fiber 6 when release is evoked exclusively from a type-Ib

terminal. **E**, Bar charts show the average amplitude of the second EJC relative to the first (N=25, 27, 8 & 6), and the mid-train EJC relative to the first (N=25, 27, 8 & 6). In each chart, a one-way ANOVA was applied ($P<0.05$ overall), with Holm Sidak *post hoc* *$P<0.01$. Paired pulse facilitation (PPF) measurements at the start of each train show type-Is terminals depressing by a greater amount than type–Ib (PPF: Is: 15.8±0.8%, N=27; Ib: 1.8±2.7%, N=8, SEM, $P<0.001$), consistent with the greater P_{AZ} of the type-Is terminals. **F**, A histogram shows the average amplitude of the mid-train EJC (Is: N=20; Ib: N=6). All preparations in D-F in 2mM $[Ca^{2+}]_o$ HL6 with no L-glutamic acid added. Error bars in E and F show SD.

Table S1

Performance in Response to a Single Action Potential

Measure	Units	type-Is	type-Ib	Source
active zone (AZ) numbers				Fig.1
terminal volume	μm^3	90±49	310±49* S.D.	
AZ / vol. (density)	μm^{-3}	2.47±0.84	2.41±0.58 S.D.	
number of AZs		223±66	747±114 p.e.	
number of T-bars		59±24	421±62 p.e.	Fig.S1
release statistics				
quantal content (QC)		91.1±6.0	67.2±3.8* S.E.M.	
corrected QC		72.9±4.8	80.6±4.5 S.E.M.	Fig.2
active zone (AZ) performance				
average AZ release *probability* (P_{AZ})		**0.33±0.10**	**0.11±0.02** p.e.	Fig.2
glutamate				
glutamate released / SV	molecules (10^3)	9.6	6.4	
glutamate released / AP	molecules (10^5)	7.00±0.46	5.16±0.29 p.e.	
glutamate released / AZ	molecules (10^3)	3.14±0.96	0.69±0.11 p.e.	
ATP spent on glutamate / AP	molecules (10^6)	1.90±0.12	1.41±0.08 p.e.	Fig.4
Ca^{2+}				
Ca^{2+} entry / AP	ions (10^6)	2.18±0.57	3.86±0.49 p.e.	Fig.3
Ca^{2+} entry / AZ	ions (10^3)	9.77±3.87	5.17±1.02 p.e.	
ATP spent on Ca^{2+} extrusion / AP	molecules (10^6)	2.18±0.57	3.86±0.49 p.e.	Fig.4
Na^+				
terminal surface area	μm^2	234±110	568±70*	
Na^+ entry / AP	ions (10^7)	0.45±0.09	1.08±0.05 p.e.	
ATP spent on Na^+ extrusion / AP	molecules (10^6)	1.48±0.28	3.60±0.18 p.e.	Fig.4
total ATP spent / AP	molecules (10^6)	**5.56±0.65**	**8.88±0.52** p.e.	Fig.4
terminal efficiency				
glutamate released / ATP spent		**0.126±0.017**	**0.058±0.005** p.e.	Fig.4
terminal performance				
SV / Ca^{2+} (*terminal sensitivity*)	SVs (10^{-5})	3.35±0.90	2.09±0.29 p.e.	
glutamate released / Ca^{2+}	molecules (10^{-1})	3.21±0.87	1.34±0.18 p.e.	

⋆ : significant difference ($P<0.05$); S.D.: standard deviation; S.E.M.: standard error of mean; p.e.: S.E.M. error calculated using propagation of uncertainty theory. Ca^{2+} imaging data, and release values from TEVC recordings, were all collected in 2mM $[Ca^{2+}]_o$ 15mM $[Mg^{2+}]_o$ HL6.

Table S2

Long Term Performance

Measure	Units	type-Is	type-Ib	Source
terminal performance during bursts of activity				
endogenous firing frequency	Hz	7.8±0.7	20.7±0.8 * S.E.M.	Fig.S5
mid-train QC (corrected)		42.3±9.4	62.1±7.9 * S.D.	
QC / s	s^{-1} (10^2)	3.3±0.3	12.8±0.8 p.e.	
glutamate / s (Glu_{bursts} / s)	molecules/s (10^6)	3.2±0.3	8.2±0.5 p.e.	Fig.6
ATP spent on glutamate / s	molecules/s (10^6)	8.6±0.9	22.5±1.4 p.e.	Fig.6
ATP spent on Na^+ / s	molecules/s (10^6)	11.6±2.5	74.5±4.7 p.e.	Fig.6
ATP spent on Ca^{2+} / s	molecules/s (10^6)	17.0±4.7	79.9±10.5 p.e.	Fig.6
total ATP spent / s	molecules/s (10^6)	37.3±5.4	176.9±11.6 p.e.	Fig.6
terminal performance during locomotion				
relative duty cycle		0.074±0.024	0.289±0.098 *S.D.	Fig.7
duty cycle		0.21±0.03	0.83±0.12 p.e.	
AP / s	s^{-1}	1.7±0.3	17.2±2.5 p.e.	
QC / s	s^{-1} (10^2)	0.70±0.12	10.7±1.6 p.e.	
glutamate / s	molecules/s (10^6)	0.68±0.11	6.85±1.04 p.e.	Fig.7
ATP spent on glutamate / s	molecules/s (10^6)	1.83±0.30	18.7±2.8 p.e.	
ATP spent on Na^+ / s	molecules/s (10^6)	2.47±0.62	62.1±9.4 p.e.	
ATP spent on Ca^{2+} / s	molecules/s (10^6)	3.6±1.1	66.6±12.7 p.e.	
total ATP spent / s	molecules/s (10^6)	7.9±1.3	147.4±16.1 p.e.	Fig.7
average ATP / μm^3 / s	molecules/μm^3/s (10^4)	8.8±2.4	47.5±6.1 p.e.	
long term terminal efficiency				
glutamate released / ATP spent	molecules/molecules	**0.085±0.020**	**0.046±0.009** p.e.	

* : significant difference ($P<0.05$); S.D.: standard deviation; S.E.M.: standard error of mean; p.e.: S.E.M. error calculated using propagation of uncertainty theory.

Supplemental Experimental Procedures

Fly Stocks
Drosophila stocks were raised at 24 ºC on standard medium (Bloomington Drosophila Stock Center (BDSC) recipe). All measurements were performed on female third-instar larvae of a w^{1118} isogenized strain, except when using larvae containing the UAS-GCaMP5G transgene (BDSC #42038), the UAS-DsRed transgene (BDSC #6282) and the OK6-Gal4 motor neuron driver [S3].

Solutions and Chemicals
Physiological experiments were conducted in HL6 solution [S4] containing 15 mM $MgCl_2$. Chemicals and antibodies were purchased from Sigma Aldrich (St Louis, MO) except where noted: $CaCl_2$ (Cat.No.21114) and $MgCl_2$ (63020), Fluka; Trolox (238813), Sigma-Aldrich; EGTA (03777), Fluka; water (for Ca^{2+} calibrations) (00612), Fluka; Oregon Green 488 BAPTA-1 dextran 10,000 MW (OGB-1; Cat.No.O-6798, Lot No.22865W) and Alexa Fluor 647 dextran 10,000 MW (AF647, D22914), Life Technologies.

Immunohistochemistry
Larvae were fillet-dissected in Schneider's insect medium (Sigma Aldrich, S0146) on Sylgard plates, rinsed three times with chilled HL6 containing no added Ca^{2+} or glutamic acid, and then fixed with Bouin's solution (Sigma Aldrich, HT10132) for 1 minute at room temperature (RT). Preparations were then rinsed with PBS (pH 7.1) (4 x 10 minutes). Following PBS rinsing, the preparations were rinsed for 1 hour (4 x 15 minutes) in PBST (PBS containing 1% Triton X-100) to permeabilize, then incubated for 30 minutes in a blocking solution [PBS containing 2% BSA, 5% goat serum (Sigma Aldrich, G9023), 1% triton-X]. After blocking, preparations were incubated with primary antibodies (diluted with blocking solution) overnight at 4 ºC: mouse anti-Bruchpilot antibody (1:200, nc82; supernatant from DSHB Hybridoma bank) and rabbit anti-Discs Large antibody (DLG; 1:20,000; a gift from Dr. Benjamin Eaton at UTHSCSA). On the second day, after washing with PBST for 1 hour (4 x 15 minutes), preparations were incubated with fluorophore-conjugated secondary antibodies and the Cy3-conjugated goat anti-HRP antibody (1:600) for 1 hour in darkness at RT: goat anti-mouse Alexa 488 (1:400); donkey anti-rabbit Cy5 (1:200). Preparations were finally washed with PBST for 1 hour (4 x 15 minutes), mounted on glass slides with antifade reagent (SlowFade Gold, S36937, Invitrogen) and covered with 0.16-0.19 mm glass cover-slips (Corning, 2870-22).

Series of images were collected from muscle fibers #6 and #7, while stepping through the entire depth of the NMJ with an Olympus FV1000 confocal microscope with a 60X 1.42 NA oil objective. Image series were collapsed into a maximal intensity z-projection. Three lasers were used sequentially (488nm, 543nm and 635nm) and emission filters were optimized for Alexa 488, Cy3 and Cy5, respectively. No bleed-through to other channels could be detected when tested with single fluorophores on a preparation. A pinhole size of 115 µm was optimal for the three imaging channels (close to 1 Airy unit). Zoom factor and step size were optimized according to the Nyquist sampling rule and images were digitized at 10.6 pixels/µm in the X-Y plane, with a step depth of 0.2 µm. 12-bit image stacks were collected and raw data were output to imageJ [Fiji (fiji.sc; ImageJ)] for analysis. DLG positive image stacks were used to distinguish different terminal types. Boutons of type-Ib terminals were distinguished from boutons of type-Is terminals by their larger size [S5], and dense DLG-positive sub-synaptic reticulum (SSR). The "TrakEM2" plugin was used to quantify total nerve terminal volume and the "3D Objects Counter" plugin was used to count the number of nc82 positive puncta.

Electron Microscopy
Third-instar larvae were fillet dissected from a dorsal midline incision and pinned against a glass slide using metal pins attached to a surrounding magnetic sheet [S5]. The initial dissection was made in Schneider's insect medium and then immersed in a primary fixative comprising 2.5% paraformaldehyde and 2.5% glutaraldehyde in 0.1M cacodylate buffer. The dissected larva was then post-fixed in 2% OsO_4 in 0.1M veronal-acetate buffer and processed for EM, as previously reported [S6, S7]. Sections were cut serially at 100 nm from embedded specimens (either transversely or longitudinally) and stained with uranyl acetate and lead citrate. Images were captured using a Gatan Orius 832 11 MB camera with a Philips Tecnai 12 electron microscope operated at 80 kV. Location of muscle fiber #6 of segment #4 was facilitated by trimming the block to allow identification of the major axes of the larva in each section. Longitudinal section series provided a means to image more boutons from a limited number of sections than did transverse sections, and after initial trials longitudinal sections were used for all reconstructions. Series of 500-600 sections were cut of which 100-200 were used to make each reconstruction. Image series collected at a magnification of 11,500 were assembled online as montages using software (Micrograph, Gatan Inc.) and then registered in a vertical series using the TrakEM2 plugin for Fiji (http://fiji.sc/) [S8]. MN terminals were reconstructed in three dimensions using additional software (Reconstruct; [S9] downloaded from http://synapses.bu.edu/tools/history.htm). Estimates of terminal volume, synaptic vesicle diameter, AZ number and AZ T-bar number were made, and their numbers recorded and annotated in Excel. A previous ultrastructural study in *Canton*

Special larvae determined average SV outer diameter to be greatest in type-Is terminals (Is: 45.0±0.4 nm; Ib: 38.5±0.3 nm; P<0.001) [S10].

Electrophysiology

Electrophysiology in conjunction with electron microscopy was used to estimate the average probability of release from AZs (P_{AZ}) because optical techniques using fluorescent Ca^{2+} reporters targeted to the postsynaptic membrane, while they generate finely dissected probability maps, do not have the capacity to resolve individual release site probability at the *Drosophila* NMJ. They can be used to quantify the probability of fluorescent events that appear to arise from the same postsynaptic locus, but the limitations of light microscopy prohibit equating these estimates to individual release site probability. The major limitation stems from projecting the 3D structure of the postsynaptic fluorescent loci surrounding boutons onto a single plane, such that events arising from several independent postsynaptic sites can appear to arise from a single locus.

Larval fillet dissections were performed in chilled HL6 on Sylgard plates (Dow Corning, Sylgard 184 Silicone Elastomer) as illustrated by Rossano and Macleod [S11]. Measurements were made between 20 and 60 minutes after transecting the segmental nerves. Measurements were performed on body wall muscle fiber #6 of segment #4 under the 20X water immersion objective of an Olympus BXWI microscope that allowed unequivocal identification of fibers. Signals were detected, digitized and recorded using an Axoclamp 900A amplifier (Molecular Devices; Sunnyvale, CA) connected to a 4/35 PowerLab (ADInstruments; Colorado Springs, CO) and a PC running LabChart v8.0. Micropipettes were pulled from borosilicate capillary tubing (Cat.No. BF15086-10, Sutter Instruments) on a Flaming/Brown P-97 micropipette puller, and filled with a 1:1 mixture of 3 M KCl and 3 M K-acetate. Unless otherwise indicated, recordings were made in Hemolymph-Like solution #6 (HL6) which contains 15mM $[Mg^{2+}]_o$ [S4]. MNSNb/d-Is innervates seven muscle fibers in addition to muscle fiber #6 [S12]. MN6/7-Ib innervates only muscle fibers #6 and #7, a subset of those innervated by MNSNb/d-Is [S13, S14]. A recording electrode (micropipette) tip in muscle fiber #6 and a second in #13 reveals that action potentials (APs) can be elicited in just one MN axon, using graded stimuli to the nerve that reach the threshold for exciting one MN but not the other, and this allows for release to be evoked from a single identified MN terminal on muscle fiber #6 [S15, S16].

Current Clamp: Under conditions of low extracellular Ca^{2+} concentration ($[Ca^{2+}]_o$), such as when quantifying the Ca^{2+} dependence of release, current clamp mode was used as the Excitatory Junction potentials (EJPs) did not approach the reversal potential and so the amplitudes of EJPs could be corrected without much risk that the process of correction for non-linear summation [S17] would introduce a large degree of error. A 0.1 gain head-stage was always used for recording from fiber #6. Average micropipette resistance was ~50 MOhms. Peak-to-peak noise was <0.15 mV after 5 kHz low-pass filtering. Only records from muscle fibers that maintained a Resting Membrane Potential (RMP) of greater than -60 mV were analyzed. Quantal Content (QC) was calculated using **Equation S.1**:

$$QC = \text{average EJP amplitude} / \text{average mEJP amplitude} \quad (S.1)$$

where average EJP amplitude is the average amplitude of 30 consecutive Excitatory Junction Potential (EJPs) (including release failures) and average mEJP amplitude is the average amplitude of 30 consecutive miniature EJPs (mEJPs). However, two adjustments were made to average EJP and mEJP amplitudes to obtain the best possible estimates of QC; i) average EJP amplitude was corrected for non-linear summation [S17], and, ii) average mEJP amplitude was adjusted according to the terminal type for which QC was being calculated. The second correction accommodates for the fact that type-Is terminals give rise to significantly larger mEJPs. Studies using extracellular focal (macropatch) micropipettes have revealed that quantal size is an average of ~50% greater in type-Is [S10, S18, S19], but the origin of mEJPs cannot be discriminated with an intracellular micropipette used in this study. We assumed that our estimates of quantal size were made from an equal contribution (numbers) of mEJPs from each terminal. Therefore QC estimates should be corrected by multiplication by a factor of 100 / ((100+150)/2) = 0.8 for type-Is terminals and 150 / ((100+150)/2) = 1.2 for type-Ib.

Two Electrode Voltage Clamp (TEVC): Under conditions of physiological $[Ca^{2+}]_o$ TEVC was generally used (except in **Figure S2E**) to avoid inaccuracies associated with correction for non-linear summation of large synaptic potentials. The lowest threshold MN was identified under current clamp as described above, after which one of the two micropipettes was moved from muscle fiber #13 to join the second in #6 to apply TEVC (**Figure 2A**). A 0.1 gain head-stage and ~50 MOhm micropipette was used for voltage recording. A 1.0 gain head-stage and ~15 MOhm micropipette was used for current passing. Muscle fibers were clamped to -60mV, but no attempt was made to clamp fibers with an initial RMP of less than -50 mV. Records were analyzed only from muscle fibers that maintained an unclamped RMP of greater than -50 mV. TEVC was generally implemented as outlined previously [S20]. Voltage deflections were <5 mV for EJCs as large as 100 nA, and muscle fiber #6 input resistance was 5.4±3.1 MOhms (N=60; ±SD). As EJC kinetics were similar between terminal types (**Figure 2B**), EJC amplitude rather than area could be quantified as a relative measure of evoked glutamate release between terminal types. Quantal Content (QC) was calculated using equation **S.1** applied to currents. EJCs do not require correction for non-linear summation, but the same scaling factor applied to mEJP amplitudes was applied to mEJCs to accommodate for

the fact that type-Is terminals give rise to both larger mEJPs and mEJCs.

Estimating the Amount of Glutamate in a Synaptic Vesicle (SV)
The number of glutamate molecules in a SV (ε) is the product of a SV's volume and lumenal glutamate concentration. While, our EM data indicate a 2.29X greater volume for type-Is SVs suggesting a 2.29X difference in the number of glutamate molecules, estimates of absolute SV lumenal glutamate concentration are rare and acknowledge assumptions that introduce a large degree of error (e.g., [S21]). ε for SVs from different terminals was therefore derived by alternate means. A numerical simulation found that 8,000 glutamate molecules released into the synaptic cleft best recapitulated the characteristics of uni-quantal events at *Drosophila* terminals on muscle #6 [S19]. Using this nominal value of 8,000 for ε we applied the scaling factors derived from electrophysiology measurements (multiplication by: Is, 1/0.8; Ib, 1/1.2) [S10, S18, S19], to generate an estimate of ε for SVs in each terminal type (Is: 9600; Ib: 6400). Differences in glutamate receptor subunit composition beneath the two terminal types [S22] may reconcile the 129% larger SVs in type-Is terminals with the 50% larger quantal size, but in the absence of direct data on SV luminal glutamate concentration a reconciliation is not possible.

Ca^{2+} Imaging
Larval fillet dissections were performed in chilled Schneider's insect medium as illustrated previously by Rossano and Macleod (2007) [S11], and the nerve was forward-filled with a 10,000 MW dextran-conjugated Ca^{2+}-indicator (OGB-1), in constant ratio with a Ca^{2+}-insensitive fluorophore (AF647 dextran), as described previously [S23]. Ca^{2+} imaging was performed under a water-dipping 100X 1.0NA objective of an Olympus BXWI50 microscope, fitted with an EMCCD camera (Andor Technology, model DU860; South Windsor, CT) running at 100 frames-per-second. The preparation was illuminated through the microscope cube turret by a DG4 150W Xenon bulb wavelength-switcher (Sutter Instruments) (OGB-1, 470/30 nm ex., 495 nm dichroic mirror (DM); AF647, 628/40 nm ex., 660 nm DM). Emission was collected through a Sutter instruments lambda 10-B filter wheel (OGB-1, 520/35 nm em; AF647, 692/40 nm em.). Filters and dichroic mirrors were obtained from Chroma Technology (Bellows Falls, VT, USA) or Semrock (Lake Forest, IL, USA).

Calibration: Fluorescence signals were converted to $[Ca^{2+}]$ using Equation 5 of Grynkiewicz and others [S24]. Values of R_{min} were obtained *in situ* through incubation of preparations in Ca^{2+}-free HL6 with 1 mM EGTA and 100 μM BAPTA-AM (1%DMSO) for 20min (Cat.No.B6769; Invitrogen). Values of R_{max} were also obtained *in situ* through incubation of preparations in HL6 containing 10 mM Ca^{2+} and 100 μM ionomycin (I9657, Sigma) for 30 min [S2]. The K_D value used for OGB-1 dextran (1.015 μM) was determined *in vitro* by measuring its fluorescence relative to AF647 in a series of solutions with different levels of free Ca^{2+}. The series was established by blending two solutions from a Ca^{2+} calibration kit (C3008MP; Invitrogen); a low Ca^{2+} solution (10 mM K_2EGTA) and a high Ca^{2+} solution (10 mM CaEGTA). Both solutions contained 100mM KCl and 30mM MOPS, prepared in deionized water at pH 7.2. K^+ levels were supplemented with the addition of ~95 μL 1M KCl (P3911, Sigma) to 2mL to bring the osmolarirty to 340 mOsm (measured in a Vapro vapor-pressure osmometer, Model No. 5520). Free Ca^{2+} levels were determined through reference to MaxChelator (http://maxchelator.stanford.edu).

Estimation of dye loading: OGB-1 loading was determined by dividing the fluorescence intensity of AF647 (co-loaded in constant ratio with OGB-1) in the center of a bouton by the fluorescence intensity of AF647 in a glass capillary filled with the OGB-1/AF647 mixture of known concentration. The same illumination and exposure settings used for calibration measurements were used for each experiment. As the diameter of a capillary will inevitably differ from the diameter of a bouton (and bouton diameters will differ between terminals), differences in path length needed to be corrected for, especially as wide-field optics were used. The procedure was as follows: Immediately prior to the acquisition of Ca^{2+}-indicator fluorescence transients, a z-series of images of AF647 fluorescence were acquired through the bouton. Close-to spherical boutons were selected where possible and the average pixel intensity was measured in a centrally positioned 3 x 3 pixel ROI (0.75μm x 0.75μm ROI). A measurement from the plane of focus with the maximum average pixel intensity was compared to a similarly obtained measurement from the glass capillary, after measurements from both boutons and capillary were corrected as described in **Appendix S1**. Briefly, maximum fluorescence measurements were corrected according to the apparent z-dimension of the bouton (or capillary) in order to compensate for out-of-focus fluorescence that might have otherwise contributed to the intensity measurement. The smallest boutons required the greatest correction.

Estimation of the endogenous Ca^{2+} binding ratio (K_S): Most Ca^{2+} that enters a terminal is bound by endogenous buffers and as little as 1% may be free [S25]. It is this small proportion of free Ca^{2+}, available to bind OGB-1 and give rise to a fluorescence transient, that is quantified through microfluorimetry. The larger amount, bound by endogenous buffers, can only be calculated after determination of the endogenous Ca^{2+}-binding ratio (K_S). To determine K_S for each terminal we quantified the effect of different concentrations of the exogenous Ca^{2+} buffer OGB-1 on the time course of decay (τ) of $[Ca^{2+}]_I$, and $\Delta [Ca^{2+}]_i$ after a single AP, and analyzed the data in a linear-approximation of a single compartment model of

Ca^{2+} binding (**Figure S3D-S3E**) [S26, S27]. In the single compartment model τ is related to the incremental Ca^{2+} binding ratio (K'_B) in **Equation S.2** (Equation 4 of [S28]):

$$\tau = (1 + K_S + K'_B) / \gamma \qquad \text{(S.2)}$$

where the Ca^{2+} extrusion mechanism is assumed to be linear with rate constant γ. Therefore, an estimate of K_S can be obtained from the abscissa intercept of a plot of τ versus K'_B, or $1/\Delta [Ca^{2+}]_i$ versus K'_B, where the intercept equals $-(K'_S+1)$. K'_B was determined using **Equation S.3** (Equation 1 of [S26]):

$$K'_B = [\text{OGB-1}] \times K_{d,\text{OGB-1}} / [([Ca^{2+}]_{rest} + K_{d,\text{OGB-1}}) ([Ca^{2+}]_{rest} + \Delta [Ca^{2+}]_{AP} + K_{d,\text{OGB-1}})] \qquad \text{(S.3)}$$

where the Ca^{2+} dissociation constant (K_d) was determined *in vitro* for OGB-1-dextran (1.015μM; described above), and where we determined the cytosolic concentration of OGB-1 ([OGB-1]) *in situ*, (described above) and $[Ca^{2+}]_{rest}$. On average, [OGB-1] was similar between nerve terminals (Is: 27.3±5.3μM; Ib: 33.2±6.2μM), consistent with identical loading periods (205±21mins) for axons forward-filled in a common nerve. Regression of τ on K'_B (**Figure S3D)** generated K_S estimates of 82.0 (Is) and 49.0 (Ib) (Is: R^2=0.47, P=0.013; Ib: R^2=0.58, P=0.004), but the 95% confidence intervals overlapped substantially. Regression of $1/\Delta [Ca^{2+}]_i$ on K'_B (**Figure S3E)** generated inferior K_S estimates as assessed by the summed R^2 values (Is: 15.9, R^2=0.64, P=0.002; Ib: 47.7, R^2=0.25, P=0.095). K_S has been previously determined as 77 for type-Ib terminals [S29] but K_S has not previously been determined for type-Is terminals.

Estimating Na^+ Entry to Nerve Terminals

Without the ability to patch presynaptic terminals at the NMJ, or to make microfluorimetric estimates of Na^+ entry, we resorted to an established theoretical approach that utilized our morphological measurements (described in the Results section). We assumed that APs actively invades both terminals [S30] and that the AP has an amplitude of 100mV. Although both assumptions likely lead to an overestimation of Na^+ entry, they are unlikely to either inflate or diminish energy efficiency differences between terminals. Our simulations show a relatively flat dependence of efficiency estimates on surface area and AP voltage (**Figure S4D**), and the curve for type-Is terminals is almost parallel to type-Ib. To the extent that our assumptions overestimate Na^+ entry, they should overestimate Na^+ entry equally for both terminals, in which case we expect a neutral effect of inaccurate assumptions on the difference in efficiency estimates.

Fictive Locomotion Measurements

The endogenous firing frequency of each MN was determined using two intracellular micropipettes to record EJPs simultaneously from fibers #6 and #13 (**Figure 6A**) while the CPG drove patterned activity in the MNs. MNs contributing EJPs were identified using a previously described method [S2]. The instantaneous firing frequency for each MN was calculated as 1/time interval (s) between adjacent EJPs, from which we then determined the average peak firing rate over a 2 s period of the MN's most intense activity [endogenous firing rate (EFR)].

Relative Duty Cycle Measurements

The relative periods of electrical activity of the two MN terminals were estimated using an optical approach. Preparations were imaged through the water-dipping objective (60X 0.9NA) of a BXWI50 Olympus microscope equipped with a beam-splitter (Cairn Optisplit II; Cairn Research, Faversham, UK) and an EMCCD camera (DV887; Andor Technology, South Windsor, CT) running at 5 frames-per-second. Both GCaMP5G and DsRed were expressed in the cytosol using the OK6-Gal4 driver and were simultaneously excited by BDX (450-495 nm) and GYX (540-600 nm) modules of an X-Cite XLED1 illuminator through a dual-band filter (470/21 nm and 556/19 nm) and dual-band dichroic mirror (512/23 nm and 630/91 nm transmission). Emission wavelengths were monitored separately but simultaneously on different sides of the EMCCD chip behind the beam-splitter (512/25 nm and 660/20 nm emissions filters; 600 nm DM). Some recordings showed no activity, or activity in only type-Ib terminals, but only recordings showing activity in both terminal types were analyzed. Type-Is never fired without simultaneous firing in type-Ib terminals, consistent with our electrophysiological recordings (data not shown).

The Definition of Presynaptic Energy Efficiency as Output/Cost

Maxwell's definition of energy efficiency [S31], based on output relative to input, guided our conception of efficiency. At a presynaptic terminal, output is defined as the amount of neurotransmitter released and the input is the metabolic cost to reset the presynaptic terminal. For synapses as a functional unit, output is usually defined in terms of information passed from the presynaptic terminal to the postsynaptic target [S32, S33]. At the *Drosophila* NMJ, information can be defined as the reduction of uncertainty to contract muscle in response to presynaptic neurotransmitter release [S34]. However, since this

synapse is a relay synapse, information here is a discrete variable with only two states depending on whether the postsynaptic event is above threshold or not. Under the conditions of this study, physiological conditions, NMJs maintain a high safety factor [S35], and so only one bit of information is considered. For this reason, rather than quantify the energy efficiency of information transfer, we quantified the energy efficiency of glutamate release which is variable between terminals [S31].

Sources of Error in the Calculation of P_{AZ} and Energy Efficiency

In the process of estimating both P_{AZ} and energy efficiency a number of assumptions and approximations were inevitable. Therefore, to ensure the strongest test of our hypothesis, we adopted a conservative approach to err on the side that would diminish differences in P_{AZ} and energy efficiency. For example, all the relevant published data point to larger mEJCs originating from type-Is terminals and in incorporating this fact into our analysis it diminished our estimate of differences in P_{AZ} between terminals. Other assumptions or approximations diminished differences in energy demand between the terminals, and thus differences in energy efficiency. First, we estimated SV glutamate content based on published electrophysiological data [S19] rather than SV volumes. Estimates based on electrophysiological data diminish differences in glutamate release as SV glutamate content is calculated to be only 50% larger for type-Is terminals, whereas estimates based on type-Is SVs that are 129% larger in volume would have exaggerated differences in glutamate release (assuming SV lumenal glutamate concentration is equal between terminals [S10]). Secondly, we might expect that glutamate receptor saturation [S19] and desensitization [S36] would have greater effects at type-Is terminals with their greater P_{AZ} and quantal size, and so the assumption that these influences are negligible may lead to greater underestimation of release from type-Is terminals. Thirdly, rather than assume there is no difference in K_S between terminals (**Figure S3D-3F**), we proceeded with our single best K_S estimates for the two terminal types which may have exaggerated the amount of Ca^{2+} entering type-Is terminals and thus the amount of ATP required to extrude the Ca^{2+}. Lastly, similar to previous studies, our estimates only considered activity-dependent cost [S37] but not the costs at rest [S38] which will be smaller for type-Is terminals. The smaller type-Is terminal surface area would obligate a lower cost to maintain the resting membrane potential and lipid turnover [S38]. Also, the smaller volume of mitochondria per unit volume of cytoplasm (density) in type-Is terminals [S5] would obligate a lower cost associated with mitochondrial proton leak [S38]. Therefore, without incorporating fixed costs at rest into our estimates we may have further underestimated differences in energy efficiency between terminal types. Despite such a conservative approach, the estimated differences in P_{AZ} and energy efficiency between terminals were substantial underlining the robust nature of these differences.

Calculation of Postsynaptic Energy Consumption at the NMJ

Postsynaptic energy consumption associated with postsynaptic synaptic currents can be calculated from an estimate of the total charge that crosses the membrane which is the product of the amplitude and decay time constant of EJCs [S39]. If we assume that all current is carried by sodium ions (Na^+), then energy consumption will equal one-third of the total Na^+ charge, as Na^+ is extruded by the Na^+/K^+ ATPase using one molecule of ATP to pump 3 Na^+. Therefore, the numbers of ATP molecules required to remove postsynaptic Na^+ after a single AP triggers release from either terminal are: Is 8.16×10^8, and, Ib 5.18×10^8. This is a rough estimate resting on simplifying assumptions that are difficult to defend, such as assuming that glutamate receptors under the different terminal types have the same subunit composition with the same glutamate binding affinity, unitary conductance and permeabilities to Na^+ relative to Ca^{2+}, yet this is clearly not the case [S22]. Never-the-less, it would appear that the amount of energy consumed on the postsynaptic side of the synapse is much higher than on the presynaptic side; perhaps 100 fold greater.

Statistical Analysis and Data Presentation

Tests were performed using SigmaStat 3.5 (integrated with SigmaPlot 10). Significance was assessed with an α of <0.05. Paired Student's t-tests were performed when comparisons were made between terminal pairs in the same preparation. ANOVA was performed when multiple comparisons were applied and an overall α of <0.05 was required for significance. Parametric or non-parametric post-hoc tests were applied according to the outcome of tests for normalcy, and described in the text. Propagation of uncertainty theory [S40] was used to calculate the standard error of means based on measurements combined from different experiments.

Appendix S1

Correcting Fluorescence Measurements for Limitation in Axial Resolution.

Summary of the Approach

Consider a hypothetical sphere/bouton with a uniform radiant energy density, of diameter "bouton_size". When an image is taken of the bouton, each point in the object contributes light to the image in a manner determined by the point spread function (psf). The mathematical process by which this is done is the 'convolution' of the real object by the psf.

When the object is symmetric in 3 dimensions the image has worse resolution in z-axis because of the characteristic asymmetry of the psf. If we assume that the xy resolution is good (not needing correction) then we can consider only correction in the z axis. Hence, a sphere (or a cylinder viewed orthogonally), uniformly filled with an indicator (AF647-dextran), reduces to a one-dimensional 'uniform' distribution of length 'bouton_size'.

The approach then is to see how changing the 'bouton_size' (keeping the luminosity from each point in the 'sphere' constant) changes the fluorescent signal measured at z=0 (focal plane). We normalize this fluorescent signal such that, for a sufficiently large bouton, the fluorescence measured at z=0 will be 1; the measurement of this fluorescent signal from the normalized boutons will be called the 'correction_factor'.

Correction Factor Derivation

Let

f= measured **f**luorescent signal

b=**b**rightness (radiant energy density) of the indicator (a constant proportional to the indicator concentration).

psf(z)= point spread function as a function of z

object(z)= a density function describing the object in one dimension; 1 when the object is present, 0 where it is absent.

Given the above, the radiant energy density over space is b. object(z).

The fluorescence of the object is the convolution of the luminescence by the psf [S41], or:

$$f = \left(b.object(z)\right) \otimes psf(z) = \int_{-\infty}^{\infty} \left(b.object(z)\right) psf(z-t).dt$$

But note that b is a constant, and hence can be taken out of the integral, so:

$$f = b\int_{-\infty}^{\infty} \left(object(z)\right) psf(z-t).dt$$

$$b = \frac{f}{\int_{-\infty}^{\infty} \left(object(z)\right) psf(z-t).dt}$$

$$b = \frac{f}{object(z) \otimes psf(z)}$$

Define “Correction_factor” as $object(z) \otimes psf(z)$

then,

$$b = \frac{f}{Correction\_factor}$$

The computational method is to calculate this “correction_factor” as a function of bouton diameter (measured in the xy plane, and assumed equal in the z direction) and an estimate of the imaging system’s axial psf. The function is plotted below.

Details:

Program "R" (http://www.r-project.org/) was used to test the effects convolution on one-dimensional 'beads' (z-axis). To calculate a “correction factor” for the fluorescent signal at z=0, we ran the “R code” shown below assuming a Gaussian psf with a standard deviation of 0.58µm (half the estimated depth-of-field for the objective used of 1.16µm; psfwidth).

R code:

```
rm(list=ls());

psfwidth <- 1.16/2; # This is the S.D. of the Gaussian - estimated at half the "depth of field" of 1160nm.

bouton_size <- 2;  # Insert the bouton, terminal or bead diameter here.

zpoints <- seq(-20,20, length.out=401);

psf<-dnorm(zpoints, sd= psfwidth);

object <- dunif(zpoints, min=- bouton_size/2, max= bouton_size/2)* bouton_size;

f <- convolve(object, psf, type = "open")/10;

z_for_convolv <- seq(-40,40,by=0.1);

f_centre_only <- f[401];

par(mfrow = c(2, 2));

plot(zpoints, object, xlim=c(-20,20), xlab="z [µm]");

plot(zpoints, psf, type="p", xlim=c(-20,20), xlab="z [µm]");

plot(z_for_convolv, f, xlim=c(-20,20), xlab="z [µm]",ylim=c(0,1));

cat("The correction factor for a bouton size", bouton_size," with psf", psfwidth, "is", f_centre_only);
```

After applying the correction factor for individual boutons with known size, we are able to quantify the relative concentration of dye loaded in the preparations based on the linear relationship between dye concentration and radiant energy density.

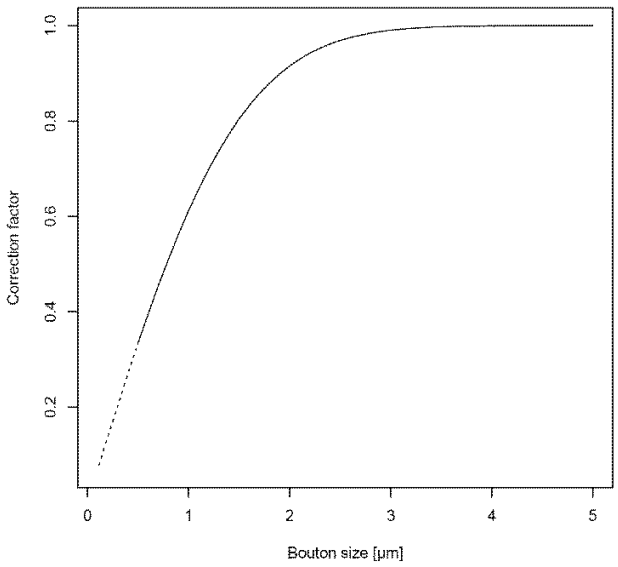

Simulation of influence of bouton diameter on correction factor.

SUPPLEMENTAL REFERENCES:

S1. Stewart, B.A., Atwood, H.L., Renger, J.J., Wang, J., and Wu, C.F. (1994). Improved stability of Drosophila larval neuromuscular preparations in haemolymph-like physiological solutions. J Comp Physiol A *175*, 179-191.

S2. Chouhan, A.K., Zhang, J., Zinsmaier, K.E., and Macleod, G.T. (2010). Presynaptic mitochondria in functionally different motor neurons exhibit similar affinities for Ca2+ but exert little influence as Ca2+ buffers at nerve firing rates in situ. J Neurosci *30*, 1869-1881.

S3. Aberle, H., Haghighi, A.P., Fetter, R.D., McCabe, B.D., Magalhaes, T.R., and Goodman, C.S. (2002). wishful thinking encodes a BMP type II receptor that regulates synaptic growth in Drosophila. Neuron *33*, 545-558.

S4. Macleod, G.T., Hegstrom-Wojtowicz, M., Charlton, M.P., and Atwood, H.L. (2002). Fast calcium signals in Drosophila motor neuron terminals. J Neurophysiol *88*, 2659-2663.

S5. Atwood, H.L., Govind, C.K., and Wu, C.F. (1993). Differential ultrastructure of synaptic terminals on ventral longitudinal abdominal muscles in Drosophila larvae. J Neurobiol *24*, 1008-1024.

S6. Meinertzhagen, I.A., and O'Neil, S.D. (1991). Synaptic organization of columnar elements in the lamina of the wild type in Drosophila melanogaster. J Comp Neurol *305*, 232-263.

S7. Meinertzhagen, I.A., and Hu, X. (1996). Evidence for site selection during synaptogenesis: the surface distribution of synaptic sites in photoreceptor terminals of the files Musca and Drosophila. Cell Mol Neurobiol *16*, 677-698.

S8. Cardona, A., Saalfeld, S., Schindelin, J., Arganda-Carreras, I., Preibisch, S., Longair, M., Tomancak, P., Hartenstein, V., and Douglas, R.J. (2012). TrakEM2 software for neural circuit reconstruction. PLoS One *7*, e38011.

S9. Fiala, J.C. (2005). Reconstruct: a free editor for serial section microscopy. J Microsc *218*, 52-61.

S10. Karunanithi, S., Marin, L., Wong, K., and Atwood, H.L. (2002). Quantal size and variation determined by vesicle size in normal and mutant Drosophila glutamatergic synapses. J Neurosci *22*, 10267-10276.

S11. Rossano, A.J., and Macleod, G.T. (2007). Loading Drosophila nerve terminals with calcium indicators. J Vis Exp, 250.

S12. Hoang, B., and Chiba, A. (2001). Single-cell analysis of Drosophila larval neuromuscular synapses. Dev Biol *229*, 55-70.

S13. Halpern, M.E., Chiba, A., Johansen, J., and Keshishian, H. (1991). Growth cone behavior underlying the development of stereotypic synaptic connections in Drosophila embryos. J Neurosci *11*, 3227-3238.

S14. Sink, H., and Whitington, P.M. (1991). Location and connectivity of abdominal motoneurons in the embryo and larva of Drosophila melanogaster. J Neurobiol *22*, 298-311.

S15. Dunn, T.W., and Mercier, A.J. (2005). Synaptic modulation by a Drosophila neuropeptide is motor neuron-specific and requires CaMKII activity. Peptides *26*, 269-276.

S16. Lnenicka, G.A., Spencer, G.M., and Keshishian, H. (2003). Effect of reduced impulse activity on the development of identified motor terminals in Drosophila larvae. J Neurobiol *54*, 337-345.

S17. McLachlan, E.M., and Martin, A.R. (1981). Non-linear summation of end-plate potentials in the frog and mouse. J Physiol *311*, 307-324.

S18. Dawson-Scully, K., Lin, Y., Imad, M., Zhang, J., Marin, L., Horne, J.A., Meinertzhagen, I.A., Karunanithi, S., Zinsmaier, K.E., and Atwood, H.L. (2007). Morphological and functional effects of altered cysteine string protein at the Drosophila larval neuromuscular junction. Synapse *61*, 1-16.

S19. Pawlu, C., DiAntonio, A., and Heckmann, M. (2004). Postfusional control of quantal current shape. Neuron *42*, 607-618.

S20. Zhang, B., and Stewart, B. (2010). Voltage-clamp analysis of synaptic transmission at the Drosophila larval neuromuscular junction. Cold Spring Harb Protoc *2010*, pdb prot5488.

S21. Riveros, N., Fiedler, J., Lagos, N., Munoz, C., and Orrego, F. (1986). Glutamate in rat brain cortex synaptic vesicles: influence of the vesicle isolation procedure. Brain Res *386*, 405-408.

S22. Marrus, S.B., Portman, S.L., Allen, M.J., Moffat, K.G., and DiAntonio, A. (2004). Differential localization of glutamate receptor subunits at the Drosophila neuromuscular junction. J Neurosci *24*, 1406-1415.

S23. Macleod, G.T. (2012). Calcium imaging at the Drosophila larval neuromuscular junction. Cold Spring Harb Protoc *2012*, 758-766.

S24. Grynkiewicz, G., Poenie, M., and Tsien, R.Y. (1985). A new generation of Ca2+ indicators with greatly improved fluorescence properties. J Biol Chem *260*, 3440-3450.

S25. Neher, E. (1995). The use of fura-2 for estimating Ca buffers and Ca fluxes. Neuropharmacology *34*, 1423-1442.
S26. Helmchen, F., Imoto, K., and Sakmann, B. (1996). Ca2+ buffering and action potential-evoked Ca2+ signaling in dendrites of pyramidal neurons. Biophys J *70*, 1069-1081.
S27. Neher, E., and Augustine, G.J. (1992). Calcium gradients and buffers in bovine chromaffin cells. J Physiol *450*, 273-301.
S28. Guan, B., Hartmann, B., Kho, Y.H., Gorczyca, M., and Budnik, V. (1996). The Drosophila tumor suppressor gene, dlg, is involved in structural plasticity at a glutamatergic synapse. Curr Biol *6*, 695-706.
S29. He, T., and Lnenicka, G.A. (2011). Ca(2)+ buffering at a drosophila larval synaptic terminal. Synapse *65*, 687-693.
S30. Ford, K.J., and Davis, G.W. (2014). Archaerhodopsin voltage imaging: synaptic calcium and BK channels stabilize action potential repolarization at the Drosophila neuromuscular junction. J Neurosci *34*, 14517-14525.
S31. Leff, H.S., and Rex, A.F. (1990). Maxwell's demon : entropy, information, computing, (Princeton, N.J.: Princeton University Press).
S32. Harris, J.J., Jolivet, R., and Attwell, D. (2012). Synaptic energy use and supply. Neuron *75*, 762-777.
S33. Niven, J.E., Anderson, J.C., and Laughlin, S.B. (2007). Fly photoreceptors demonstrate energy-information trade-offs in neural coding. PLoS Biol *5*, e116.
S34. Sterling, P., Laughlin, S., and ebrary Inc. Principles of neural design. p. 1 online resource.
S35. Wood, S.J., and Slater, C.R. (2001). Safety factor at the neuromuscular junction. Prog Neurobiol *64*, 393-429.
S36. Adelsberger, H., Heckmann, M., and Dudel, J. (1997). The amplitude of quantal currents is reduced during short-term depression at neuromuscular synapses in Drosophila. Neurosci Lett *225*, 5-8.
S37. Liotta, A., Rosner, J., Huchzermeyer, C., Wojtowicz, A., Kann, O., Schmitz, D., Heinemann, U., and Kovacs, R. (2012). Energy demand of synaptic transmission at the hippocampal Schaffer-collateral synapse. J Cereb Blood Flow Metab *32*, 2076-2083.
S38. Engl, E., and Attwell, D. (2015). Non-signalling energy use in the brain. J Physiol *593*, 3417-3429.
S39. Carter, B.C., and Bean, B.P. (2009). Sodium entry during action potentials of mammalian neurons: incomplete inactivation and reduced metabolic efficiency in fast-spiking neurons. Neuron *64*, 898-909.
S40. Taylor, J.R. (1997). Error Analysis: the study of uncertainties in physical measurements., Second Edition, (Sausalito, CA: University Science Books).
S41. Hecht, E. (1987). 11.3.2 The Convolution Integral. In Optics, Second Edition. (Wokingham: Addison-Wesley), pp. 486-493.